

**Design Parameter Modeling and Beam Quality**

**Analysis of 850 nm GaAs/AlGaAs**

**Semiconductor Lasers**

**Jung-Tack Yang**

**The Graduate School**

**Yonsei University**

**Department of Electrical and Electronic Engineering**

**Design Parameter Modeling and Beam Quality  
Analysis of 850 nm GaAs/AlGaAs  
Semiconductor Lasers**

by

***Jung-Tack Yang***

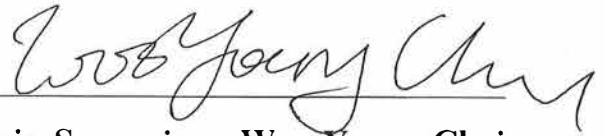
A Dissertation

Submitted to the Department of Electrical and Electronic Engineering  
and the Graduate School of Yonsei University  
in partial fulfillment of the requirements for the degree of

**Doctor of Philosophy**

**December 2023**

This certifies that the dissertation of Jung-Tack Yang is approved.



Thesis Supervisor: Woo-Young Choi



Sang-Kook Han



Hong-Goo Kang



Younghyun Kim



Minkyu Kim

**The Graduate School**

**Yonsei University**

**December 2023**

# Table of Contents

<b>Table of Contents</b> .....	i
<b>List of Figures</b> .....	iv
<b>Abstract</b> .....	viii
<b>1. Introduction</b> .....	1
1.1. Lasers .....	1
1.2. Semiconductor Lasers.....	3
1.2.1. Edge-Emitting Lasers .....	5
1.3. Beam Quality .....	8
1.3.1. Standards of Beam Quality .....	9
1.4. Simulation Works .....	11
1.5. Outline of Dissertation .....	12
<b>2. Background</b> .....	15
2.1. Carrier Transition .....	15
2.1.1. Radiative Recombination .....	17
2.1.2. Non-Radiative Recombination .....	19
2.2. Rate of Carrier Transition .....	21
2.3. Threshold and Steady State in Lasers .....	24
2.3.1. Material and Modal Gain .....	24

2.3.2. L-I Characteristic .....	29
2.4. Deep Learning Technique .....	30
2.4.1. Activation and Loss Function .....	32
2.4.2. Training and Testing .....	34
<b>3. High-Power Semiconductor Laser Structure for Improving</b>	
<b>Beam Quality</b> .....	35
3.1. Far-Field Blooming .....	37
3.2. Pedestal Structure .....	38
3.3. Double Pedestal Structure .....	42
3.3.1. Epitaxial Lift-Off Technique .....	43
3.3.2. Results .....	45
3.4. Summary .....	48
<b>4. Single Mode Semiconductor Laser</b> .....	49
4.1. Fabricated 850 nm GaAs/AlGaAs Single Quantum-Well	
SMSL .....	51
4.2. Kink and Far-Field Pattern Analysis .....	54
4.3. Summary .....	62
<b>5. Optimizing Structure for Kink Suppression</b> .....	63
5.1. Design Parameters Extraction and Modeling .....	64
5.1.1. Device Structure .....	66
5.1.2. Internal Loss Modeling .....	68
5.1.3. Auger and FCA Coefficients Modeling Based on	
DNNs .....	71
5.1.4. Algorithm and DNN Structure .....	73
5.1.5. Results .....	79

5.2. Simulation Validation of $W=3\ \mu\text{m}$ .....	85
5.3. Optimizing Structure .....	90
5.4. Summary .....	93
<b>6. Conclusion</b> .....	<b>94</b>
<b>Bibliography</b> .....	<b>96</b>
<b>Abstract (In Korean)</b> .....	<b>109</b>
<b>List of Publications</b> .....	<b>111</b>

# List of Figures

<b>Fig.1-1.</b> Simple schematic diagram: (a) VCSEL, (b) edge-emitting laser. ....	4
<b>Fig.1-2.</b> Simple cross-sectional schematic of edge-emitting laser. ....	6
<b>Fig.1-3.</b> Semiconductor laser packages: (a) TO-Can, (b) submount, (c) bar, (d) stack packages. ....	7
<b>Fig.1-4.</b> Laser diode/stack fiber coupling schematic. ....	8
<b>Fig.1-5.</b> Schematic of Gaussian beam. ....	10
<b>Fig.2-1.</b> Carrier transitions between conduction and valence bands. ....	16
<b>Fig.2-2.</b> Auger recombination: CCCH, CHHS and CHHL processes. ....	20
<b>Fig.2-3.</b> Reservoir analogy above threshold where water level has risen to the spillway. ....	21
<b>Fig.2-4.</b> Gain spectrum versus carrier density in bulk GaAs. Indicated values are the sheet carrier densities: $\times 10^{12} \text{ cm}^{-2}$ . ....	25
<b>Fig.2-5.</b> Generic cross-sectional schematic of laser cavity. ....	27
<b>Fig.2-6.</b> Material gain versus carrier density and carrier density versus input current. ....	28
<b>Fig.2-7.</b> Simple schematic structure of DNNs. ....	31
<b>Fig.3-1.</b> Reported results of BPP from international journals and conferences. ....	36
<b>Fig. 3-2.</b> Schematic semiconductor laser structure including heatsink: (a) general type, (b) applying pedestal structure. ....	40
<b>Fig. 3-3.</b> Calculated L-I characteristics of high-order modes with increasing current: (a) pedestal structure, (b) original structure, ....	

and (c) divergence angle of far-field pattern of original and pedestal structure, and (d) L-I characteristics and quantum well temperature of original and pedestal structure. .... 41

**Fig. 3-4.** Fabrication process of DP structure with ELO technique: (a) semiconductor laser applying pedestal structure, (b) bonding of the top metal, (c) removal of substrate by ELO technique, (d) construction of the N-contact applying bottom pedestal structure, (e), (f) construction of bottom and top heat-sink. 44

**Fig. 3-5.** Cross-sectional schematic of semiconductor laser applying double pedestal structure, and performance of the original device compared to the device with the application of pedestal and double pedestal structures: (b) L-I characteristics and quantum well temperature, (c) thermal distribution, and (d) divergence angle of far-field pattern of double pedestal structure with different contact size. .... 47

**Fig. 4-1.** Fabricated single quantum well semiconductor laser based on GaAs/AlGaAs: (a) cross-section, (b) SEM image. .... 52

**Fig. 4-2.** Measured L-I characteristics: (a) L= 1200, (b) 1500, (c) 1800  $\mu\text{m}$ . .... 53

**Fig. 4-3.** Measured divergence angles: (a) L= 1200, (b) 1500, (c) 1800  $\mu\text{m}$ . .... 56

**Fig. 4-4.** Measured far-field patterns in three scenarios: before the kink occurrence, after the kink occurrence, and within kink occurrence: (a) L= 1200, (b) 1500, (c) 1800  $\mu\text{m}$ . .... 57

**Fig. 4-5.** Measured resonance wavelengths of W= 3  $\mu\text{m}$  at T= 273, 293, 313, 333 K: (a) L= 1200, (b) 1500, (c) 1800  $\mu\text{m}$ , and (d) relationship between temperature and resonance wavelength. .... 59

**Fig. 4-6.** Measured resonance wavelength and calculated inner temperature of the devices: (a) L= 1200, (b) 1500, (c) 1800



$\mu\text{m}$ . .....	60
<b>Fig. 4-7.</b> Measured resonance wavelength and calculated inner temperature of the devices: (a) $L= 1200$ , (b) $1500$ , (c) $1800$ $\mu\text{m}$ . .....	61
<b>Fig. 5-1.</b> Fabricated $850$ nm GaAs/AlGaAs multi-quantum well semiconductor laser: (a) cross-sectional structure and (b) L-I characteristics at $293, 303, 313, 323$ K. ....	67
<b>Fig. 5-2.</b> (a) Measured $1/\eta_d$ versus $L= 300, 700, 1100$ $\mu\text{m}$ and (b) extracted internal loss versus temperature at $293, 303, 313, 323$ K. ....	70
<b>Fig. 5-3.</b> Consecutive schematic structure of DNN. ....	76
<b>Fig. 5-4.</b> Overall process of parameter extraction. ....	77
<b>Fig. 5-5.</b> Process of iteration for finding testing dataset which has minimum testing loss. ....	78
<b>Fig. 5-6.</b> Loss curves of DNN#1 of (a) training and (b) testing. ....	81
<b>Fig. 5-7.</b> Extracted values and curve of Auger coefficient. ....	82
<b>Fig. 5-8.</b> Loss curves of DNN#2 of (a) training and (b) testing. ....	83
<b>Fig. 5-9.</b> L-I characteristics of simulation and measurement at (a) $293$ , (b) $303$ , (c) $313$ and (d) $323$ K using extracted parameters. ....	84
<b>Fig. 5-10.</b> Fabricated $850$ nm GaAs/AlGaAs multi-quantum well semiconductor laser of $W= 3$ $\mu\text{m}$ : Measured L-I characteristic and insets of far-field pattern at $120$ and $220$ mW. ....	87
<b>Fig. 5-11.</b> (a) Measured divergence angle with increasing output power and (b) measured far-field patterns at $40$ and $60$ mW, simulated far-field pattern at $40$ mW. ....	88
<b>Fig. 5-12.</b> Measured (a) Spectrum and (b) measured and simulated inner temperature of $W= 3$ $\mu\text{m}$ . ....	89

**Fig. 5-13.** (a) Cross sectional diagram and (b) Simulated output power of 1<sup>st</sup> order mode generation with increasing  $t$ . ..... 92

## **Abstract**

# **Design Parameter Modeling and Beam Quality**

## **Analysis of 850 nm GaAs/AlGaAs**

### **Semiconductor Lasers**

***Jung-Tack Yang***

Dept. of Electrical and Electronic Engineering

The Graduate School

Yonsei University

This dissertation focuses on the research methodology for the enhancement of both the output and beam quality of 850 nm GaAs/AlGaAs semiconductor lasers, emphasizing device structure studies and simulation-based structural optimization. Semiconductor lasers are suitable for mass production, cost-effective, and widely used in systems requiring compact light sources. However, high-power

semiconductor lasers suffer from poor beam quality due to the generation of multiple modes, limiting their direct use in high-power systems. They are often employed as pumping sources for other lasers, such as gas or fiber lasers. The motivation for this research arises from the prospect of achieving both high output and beam quality in semiconductor lasers, making them directly applicable and significantly improving efficiency in terms of cost and size in systems.

In the case of high-power semiconductor lasers, far-field blooming occurs as the output increases, leading to a degradation in beam quality. To address this, we designed a double pedestal structure that efficiently dissipates heat from the upper and lower centers, resulting in improved optical output and beam quality. Additionally, inspired by the possibility of achieving high output through a laser bar composed of single-mode semiconductor lasers (SMSL), we proceeded to fabricate and analyze a 850 nm GaAs/AlGaAs SMSL. Although we successfully fabricated devices with an output close to the targeted 1 W, the occurrence of nonlinear phenomena, such as kink, led to a deterioration in beam quality. To mitigate this issue, we conducted a structural optimization study. For precise simulation construction, we measured and accurately extracted and modeled design parameters using deep learning. The reliability of the constructed simulation was verified

through comparisons with measurement data. We propose an optimized structure that minimizes kink occurrence. The optimization study is expected to be consistently applicable not only to the device used in this dissertation but also to other components.

---

**Keywords:** Semiconductor laser, double pedestal, SMSL, deep learning, DNN, design parameter extraction, L-I characteristic, internal loss, Auger coefficient, FCA coefficient, kink, far-field pattern, beam quality.

# **1. Introduction**

## **1.1. Lasers**

Lasers are source devices that utilize the stimulated emission of light energy corresponding to the energy difference between two energy levels when carriers at higher energy levels in the molecules constituting the laser fall to lower energy levels. They come in various types, including solid-state, gas, fiber, semiconductor. Building the device known as a laser typically requires the following fundamental elements: an optical gain medium to generate photons and a resonant cavity composed of mirrors, positioned in the front and back, to resonate the generated photons. Photons are generated by carriers excited from a pumping source within the gain medium. As coherent light builds up through resonance within the cavity, lasing occurs when the generated gain matches the surrounding losses. Lasers are categorized into continuous wave (CW) and pulsed wave (PW) types, depending on their intended use. They find applications across a wide range of power levels, from low to high. Additionally, due to their ability to focus into small spot sizes, lasers are particularly valuable for precision tasks. As a result, lasers are utilized in diverse fields including

space communication, medical instruments, and micro-machining [1-5].

## 1.2. Semiconductor Lasers

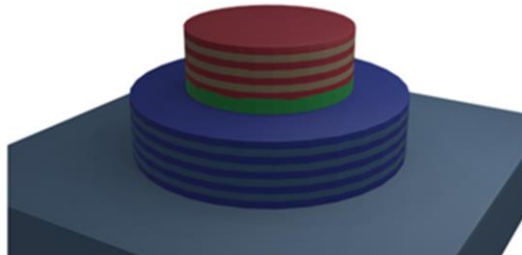
Semiconductor lasers are lasers that use electrical energy as a pumping source and are primarily composed of III-V materials with a direct band gap. Unlike other laser systems, semiconductor lasers have the advantage of being mass-produced, compact in size, and exhibiting good power conversion efficiency, meaning they produce a high output optical power relative to the input electrical power [6-8]. However, a drawback is that in high-power operations, they tend to produce many lateral modes, leading to reduced beam quality [9-10]. As a result, in applications requiring precision work at high power levels, they are often used as a pumping light source for other laser systems [11-14]. Additionally, they find widespread use in fields such as precision machining, telecommunications and medical instruments [15-21], as well as in LiDAR [22-24] and facial recognition sensors [25-26].

Semiconductor lasers can be categorized into VCSELs (Vertical-cavity surface-emitting laser) and edge-emitting lasers based on whether the mirrors are oriented in the vertical or longitudinal direction which are shown in Fig.1-1. In the case of VCSEL, Bragg patterns are introduced above and below the active region, creating AR (Anti-reflection) and HR (High-reflection) mirrors. As a result, the laser beam



is emitted from the upper (AR) surface. On the other hand, edge-emitting lasers are cut along the facet in front and behind the active region, and AR and HR coatings are applied to the cut facet to form mirrors. In this case, the light is emitted from the AR-coated portion. In this dissertation, 850 nm GaAs/AlGaAs edge-emitting lasers are investigated.

(a)



(b)

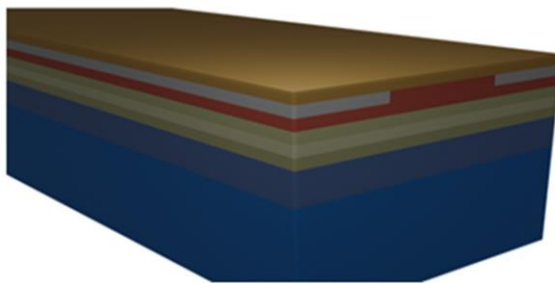


Fig.1-1. Simple schematic diagram: (a) VCSEL, (b) edge-emitting laser .

### **1.2.1 Edge-Emitting Lasers**

Edge-emitting lasers can have cavity lengths extended to several millimeters, which has led to significant development and interest as high-power lasers, unlike VCSELs. The simple cross-sectional schematic of the device is depicted in Fig. 1-2. The active region consists of lightly doped quantum wells and barriers. Above and below, materials with a larger bandgap, P- and N-doped respectively, form cladding to enable vertical waveguide. At the top of the P-cladding layer, the stripe width is set according to the lateral size of the beam to be emitted. Etching is then performed to create a mesa, while insulating materials are applied on the sides to deposit the current block layer. Through the mesa, lateral ridge waveguide is achieved based on the effective refractive index difference between the center and sides when viewed laterally. Edge-emitting lasers come in various package types depending on their output and purpose. These include TO cans for low power, submount packages commonly used for high power, and various packages like laser bars and stacks for applications requiring several hundred watts of power and they are shown in Fig.1-3.

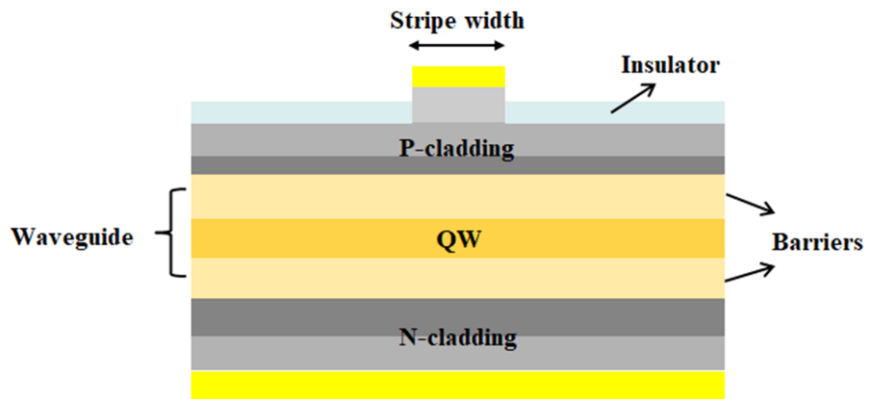


Fig.1-2. Simple cross-sectional schematic of edge-emitting laser.

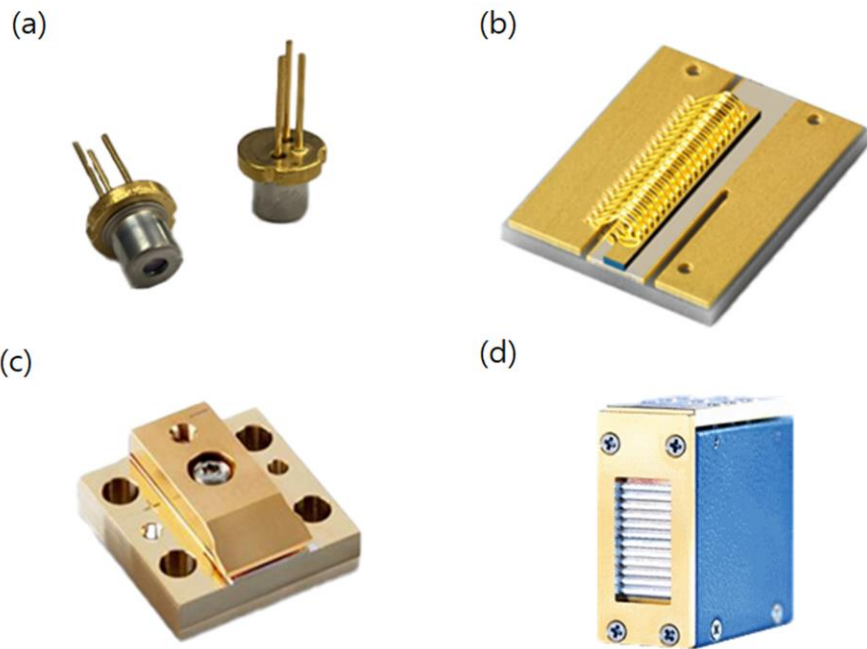


Fig.1-3. Semiconductor laser packages: (a) TO-Can, (b) submount [27], (c) bar [28], (d) stack packages[29].

### 1.3. Beam Quality

The light generated through a semiconductor laser is primarily transmitted through optical fibers shown in Fig. 1-4. Therefore, the optical coupling efficiency between the device and the optical fiber is crucial. The factor that determines the coupling efficiency is the beam quality of the light emitted from the device, which is typically measured using parameters like Beam Parameter Product (BPP) and  $M^2$  [30-32].

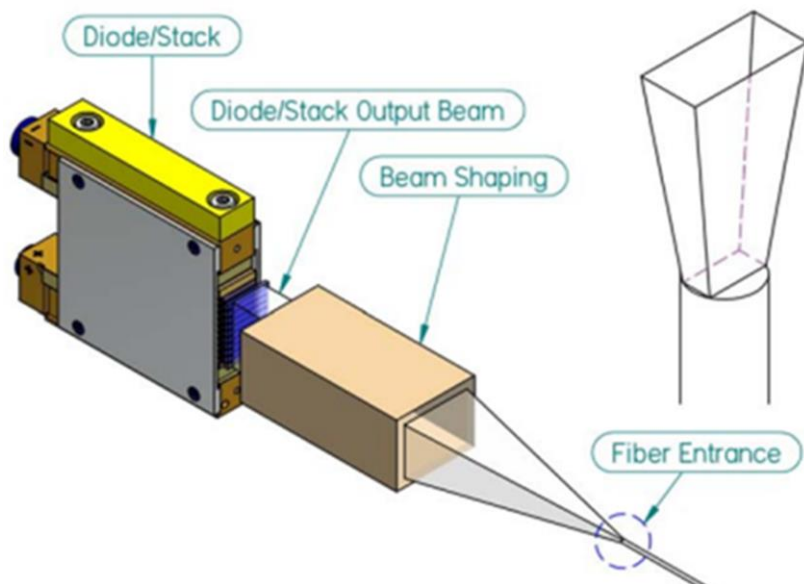


Fig.1-4. Laser diode/stack fiber coupling schematic [31].

### 1.3.1 Standards of Beam Quality

Laser beams are typically generated in the form of Gaussian beams, which exhibit the characteristic that the lateral distribution of optical intensity in the beam can be represented using a Gaussian function. In Fig.1-5, a Gaussian beam is represented as having a waist with a diameter of  $2w_o$  at a spot where it exhibits a divergence angle of  $2\theta_o$ . When considering the wavelength of this beam as  $\lambda$ , the relationship between the waist and divergence angle can be described by the following equation:

$$2w_o \times 2\theta_o = \frac{4\lambda}{\pi}. \quad (1.1)$$

For beams that are not Gaussian and include multi-modes rather than single modes, assuming the same waist, the divergence angle can be greater than  $2\theta_o$  due to higher-order modes. Therefore, the parameter known as the beam parameter product (BPP) is often used as a primary criterion for defining the beam quality of light generated from semiconductor lasers. It is defined as:

$$BPP = w \times \theta. \quad (1.2)$$

This definition becomes challenging when there are various semiconductor lasers with different wavelengths, making it difficult to compare beam quality. Therefore, the normalized  $M^2$  scale, which is

obtained by dividing the actual beam's BPP by the BPP of a Gaussian beam, is often used.

$$M^2 = \frac{BPP_{device}}{BPP_{Gaussian}} = \frac{w \times \theta}{\frac{\lambda}{\pi}}. \quad (1.3)$$

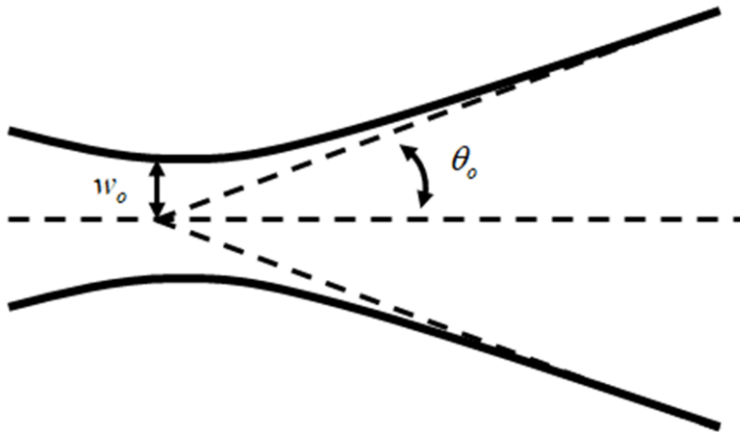


Fig.1-5. Schematic of Gaussian beam.

## **1.4. Simulation Works**

Since direct device fabrication and measurement were challenging, precise component analysis through simulation played a crucial role in our research. Accurate simulations allow us to investigate aspects that are challenging to measure and analyze experimentally. They enhance the accuracy of design for performance improvement and can significantly reduce both time and costs. To achieve accurate simulations, it is essential to precisely model the design parameters that determine the performance of the components within the simulation.

For our semiconductor laser simulations, the simulation tool should possess self-consistent capabilities for electrical, optical, and thermal simulations. In our works, we conducted simulations using the commercial TCAD tool for semiconductor lasers, PICS3D [33]. This tool allows us to perform various analyses beyond the basic performance metrics measured experimentally, such as L-I and I-V characteristics and far-field patterns. It also enables analyses of near-field patterns, internal temperature distributions, current flow, and more within the device.



## **1.5. Outline of Dissertation**

This dissertation focuses on the component structure research for performance enhancement of 850 nm GaAs/AlGaAs-based semiconductor lasers, including beam quality. The study emphasizes precise design parameter extraction and modeling for accurate simulations, forming the basis for structural optimization. It proposes a structure to overcome factors degrading beam quality in high-power semiconductor lasers and addresses the beam quality limitations arising from the occurrence of multiple modes by fabricating and measuring single-mode semiconductor lasers for analysis. The nonlinear phenomena occurring in these lasers are analyzed, and structural optimization studies are conducted to suppress them. To facilitate structural optimization, accurate design parameters are extracted to construct precise simulations, leading to the proposal of an optimized structure.

Chapter 2 provides the background necessary for understanding the research conducted in this dissertation. To generate light in a semiconductor laser, it's crucial to understand the carrier transitions originating from an electrical pumping source. In chapter 2.1, we introduce carrier transitions in semiconductor lasers. Chapter 2.2

presents a theoretical approach to understanding the changes in carriers and photons due to carrier transitions. Chapter 2.3 explains material and modal gain, which defines how photons are generated from injected carriers in a laser. Based on this, we theoretically derive the relationship between the injected current and emitted optical power in a semiconductor laser using resonance conditions. Lastly, in chapter 2.4, we introduce deep learning, which is applied to extract design parameters.

In Chapter 3, the dissertation introduces far-field blooming, which degrades beam quality at high outputs in high-power semiconductor lasers. It presents a pedestal structure, previously studied to alleviate this issue. Building on this, the dissertation introduces the double pedestal structure, applying the pedestal structure both above and below by utilizing the ELO technique to separate the substrate and device. This approach effectively suppresses far-field blooming, resulting in improved beam quality and output power.

In Chapter 4, an analysis of the fabricated 850 nm GaAs/AlGaAs-based single-mode semiconductor lasers is conducted. The performance is evaluated through far-field patterns, L-I characteristics, and temperature analysis. The chapter also includes an analysis of the nonlinear phenomenon, kink, occurring in the device.

Chapter 5 introduces a methodological study on structural optimization to suppress the kink that degrades beam quality. To construct precise simulations necessary for structural optimization, design parameters are measured and extracted from the actual device using deep learning. The extracted parameters are utilized to validate the reliability of the constructed simulations against measurement values. Based on this validation, a proposal for structural optimization that effectively suppresses the kink is presented.

Finally, chapter 5 serves as the conclusion and discussion section, summarizing this dissertation's key points and findings.

## **2. Background**

### **2.1. Carrier Transition**

As mentioned earlier, semiconductor lasers differ from other laser systems in that their pumping source is electrical energy. Consequently, the changes in carriers due to carrier transitions determine the changes in photons. Carrier transitions can be broadly categorized into absorption and recombination processes, each involving the absorption and emission of energy. Recombination, in turn, can be further divided into two main types: radiative recombination, which includes processes like spontaneous and stimulated recombination, resulting in the emission of light energy; and non-radiative recombination, which involves the release of thermal energy, encompassing mechanisms like Auger and Shockley-Read-Hall (SRH) recombination. These carrier transitions are shown in Fig.2-1. In chapter 2.2 and 2.3, based on the reference book [34], we analyze the rates of carrier transitions and theoretically derive the relationship between the input current of the semiconductor laser and its output optical power.

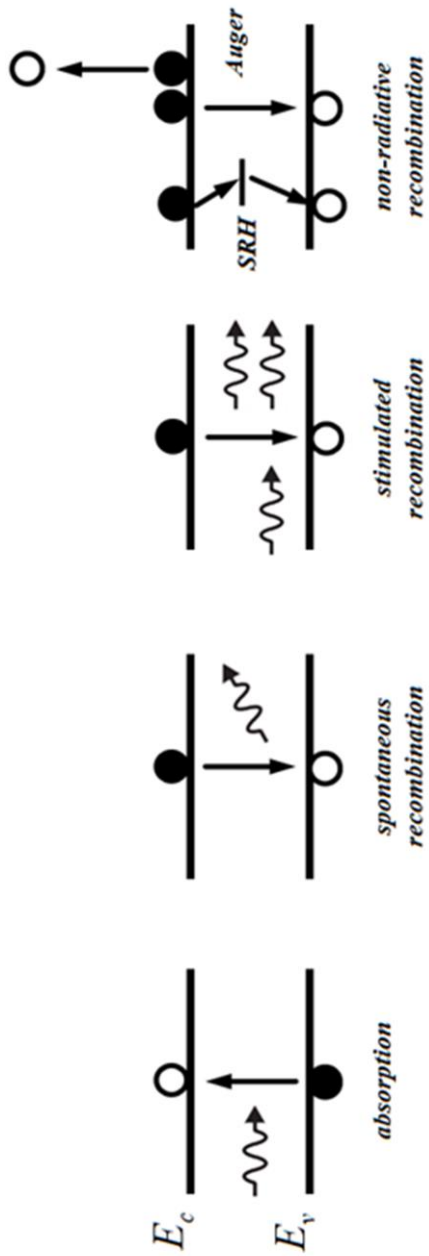


Fig.2-1. Carrier transitions between conduction and valence bands.

### **2.1.1. Radiative Recombination**

Spontaneous recombination occurs when an excited carrier transitions from the conduction band to the valence band, releasing light in the process. Spontaneous recombination is independent of the presence of light. When carriers recombine spontaneously, the generated photon has random phases and directions. This randomness in phase and direction makes spontaneous emission a fundamental process in many optical devices and natural phenomena. Stimulated recombination is a process that occurs when a material interacts with incident light. In this process, when an incoming photon interacts with an excited electron in the material, it triggers the electron to transition from a higher energy state to a lower energy state, releasing a photon in the same phase and direction as the incident photon. This results in the generation of a coherent photon, which possesses the same characteristics (phase, frequency, and direction) as the incident light. Stimulated emission is a key principle behind the amplification of light in laser devices, as it leads to the production of coherent and highly directional light beams. In the case of a semiconductor laser, when current is initially injected into the device, only spontaneous recombination occurs. During this stage, photons are generated due to spontaneous recombination processes. Among these photons, those that

match the resonance conditions within the optical cavity lead to stimulated recombination. As the injected current increases and reaches a specific threshold level (threshold current or carrier density), stimulated recombination becomes the dominant process, resulting in the lasing action of the laser. This threshold current is a critical parameter that determines when the laser transitions from spontaneous emission to stimulated emission, marking the onset of laser operation.

### **2.1.2. Non-Radiative Recombination**

SRH recombination is associated with defects or impurities in the semiconductor crystal lattice. In a semiconductor, there may be defects or impurities present in the crystal lattice structure. These defects create localized energy states within the forbidden gap of the semiconductor material. When an electron or hole encounters such a defect, it can become trapped in one of these localized energy states. When these trapped carriers recombine with carriers of the opposite type, energy is released in the form of heat, contributing to non-radiative recombination processes in semiconductor devices. Auger recombination is a process where carriers (electrons or holes) within the same energy band collide, leading to a transfer of energy among them. Figure 2-2 shows three main types of Auger recombination: CCCH, CHHS, and CHHL [34]. To explain CCCH, consider two electrons within the conduction band colliding. During this collision, one of the electrons gains extra energy and moves to a higher energy level within the conduction band, while the other electron loses some energy and recombines with the valence band. The electron that moved to the higher energy level will eventually release excess energy as thermal energy to stabilize itself, typically by transitioning to the bottom of the conduction band's energy levels. Auger recombination is



significant because it represents a non-radiative process for carriers in semiconductor materials. It involves carrier interactions and energy exchange within the material, ultimately affecting its electrical and optical properties.

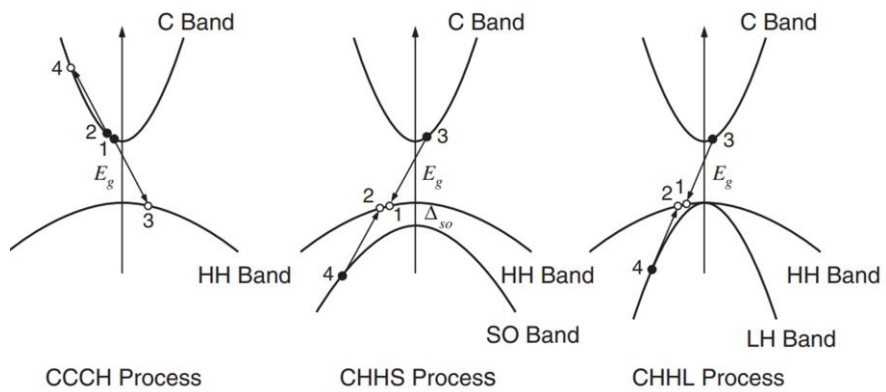


Fig.2-2. Auger recombination: CCCH, CHHS and CHHL processes [34].

## 2.2. Rate of Carrier Transition

When current is injected into a semiconductor laser, as previously mentioned, the generation of photons is determined by carrier transitions. Therefore, it is crucial to analyze the rate at which each of these transitions occurs per second. Figure 2.3 provides a metaphorical representation of the transitions when a current greater than the threshold current is injected into a semiconductor laser.  $R_l$  represents carrier leakage from the active region.  $R_{nr}$ ,  $R_{sp}$  and  $R_{st}$  represent the rates of non-radiative, spontaneous, and stimulated recombination, respectively, while  $N_{th}$  signifies the threshold carrier density.

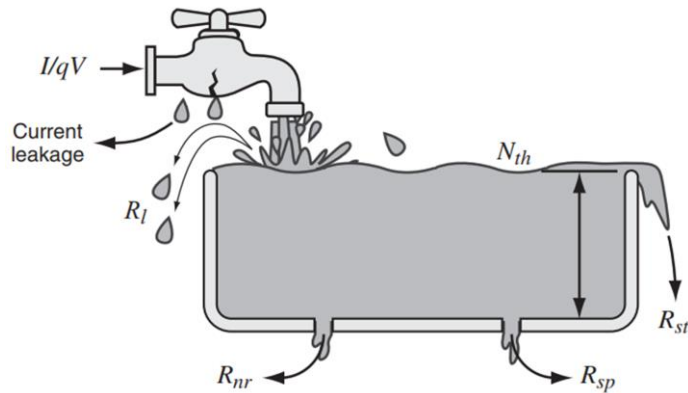


Fig.2-3. Reservoir analogy above threshold where water level has risen to the spillway [34].

The change of carrier density in the active region can be expressed as:

$$\frac{dN}{dt} = G_{gen} - R_{rec}. \quad (2.1)$$

$G_{gen}$  and  $R_{rec}$  represent the ratios of carrier density injected and recombined, respectively. Assuming the volume of the active region is  $V_o$  and the current leakage rate is  $1-\eta_i$ , the rate of carrier density injected per second,  $G_{gen}$ , can be expressed as:

$$G_{gen} = \eta_i \frac{I}{qV_o}, \quad (2.2)$$

where  $I$  is the current and  $q$  is the charge of an electron.

Recombination is subdivided into four rates, as shown in Fig. 2-D, and it can be analyzed as an approximation based on carrier density ( $N$ ) and time constant ( $\tau$ ), as expressed in the following equation as:

$$R_{rec} = R_l + R_{nr} + R_{sp} + R_{st}, \quad (2.3)$$

$$R_{rec} = \frac{N}{\tau} + R_{st}. \quad (2.4)$$

In order to increase the number of coherent photons inside a

semiconductor laser, only photons moving in the cavity's resonance direction (z-direction) can gain through stimulated emission. The increased quantity of photons at this time is expressed as:

$$N_p + \Delta N_p = N_p e^{g\Delta z}, \quad (2.5)$$

where  $N_p$  is photon density and  $g$  is material gain. When  $\Delta z$  is sufficiently small, the approximation  $e^{g\Delta z} \approx (1 + g\Delta z)$  is possible. Therefore, the increased quantity of photons and  $R_{st}$  can be expressed as:

$$\Delta N_p = N_p g \Delta z = N_p g v_g \Delta t, \quad (2.6)$$

$$R_{st} = \frac{\Delta N_p}{\Delta t} = v_g g N_p, \quad (2.7)$$

where  $v_g$  is the group velocity. Based on the derived equations (2.1), (2.2), (2.4) and (2.7), summarizing the changes in carrier density is expressed as:

$$\frac{dN}{dt} = \eta_i \frac{I}{qV_o} - \frac{N}{\tau} - v_g g N_p. \quad (2.8)$$

## **2.3. Threshold and Steady State in Lasers**

### **2.3.1. Material and Modal Gain**

To understand the increase in optical output in lasers, it's important to grasp both material gain and modal gain accurately. As mentioned earlier,  $g$  represents the material gain of the substances forming the active region of the laser. Material gain is the growth or decrease ratio of light intensity per unit length of light propagation within the material. When there are few carriers within the material, there's no population inversion upon light incidence, leading to more absorption mechanism compared to recombination mechanism, resulting in negative gain (or absorption). On the contrary, when there's a sufficient quantity of carriers within the material to achieve population inversion upon light incidence, recombination mechanism happens more prominently than absorption mechanism. This leads to positive gain, and the greater the number of carriers, the higher the gain. Figure 2-4 illustrates the gain spectrum of bulk GaAs. When light with a wavelength longer than the bandgap energy enters a material, it simply passes through. However, when light with a shorter wavelength enters, it can have positive or negative gain values depending on the magnitude of the carrier density within the material.

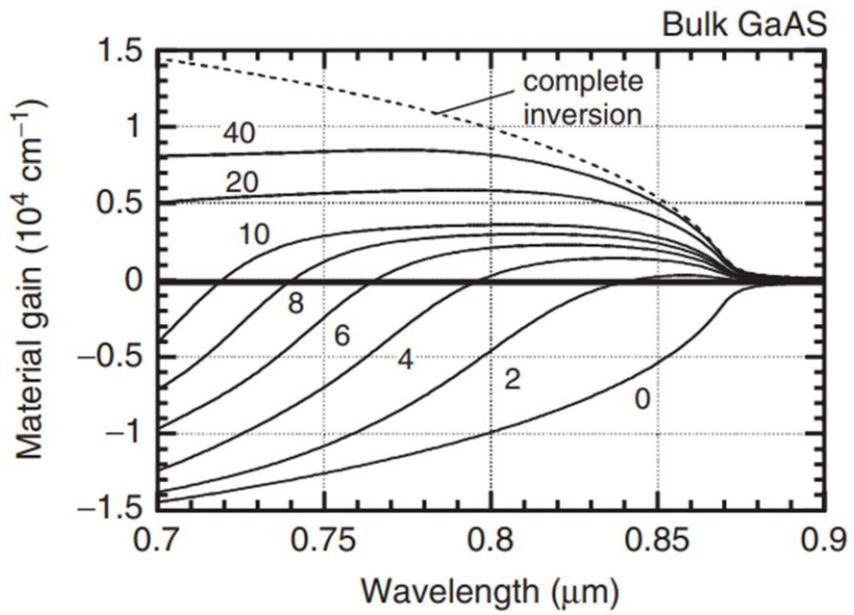


Fig.2-4. Gain spectrum versus carrier density in bulk GaAs. Indicated values are the sheet carrier densities:  $\times 10^{12} \text{ cm}^{-2}$  [34].

Figure 2-5 shows the laser cavity cross-section.  $L$  is the cavity length and each  $r_1$  and  $r_2$  is reflectivity of each facet. The electric field of the mode generated in a semiconductor laser can be represented in the  $xy$  plane using the photon distribution function,  $U(x, y)$ , as shown in the following equation as:

$$E = e_y E_o U(x, y) e^{j(\omega t - \tilde{\beta} z)}, \quad (2.9)$$

where  $e_y$  is the unit vector of TE polarization and  $E_o$  is the magnitude of field. The complex propagation constant,  $\tilde{\beta}$ , is defined as:

$$\hat{\beta} = \beta + \frac{j}{2}(\Gamma g - \alpha_i), \quad (2.10)$$

where  $\Gamma$  is the confinement factor which has the value of  $V_o / V_p$ , and  $\alpha_i$  is the internal loss, the rate at which the field's magnitude decreases per unit distance as it propagates in the  $z$ -direction. For a mode to reach the threshold for lasing, its magnitude must be preserved after completing one round trip inside the cavity. Therefore, considering what's reflected at each facet, the threshold condition can be expressed as the following equation,

$$r_1 r_2 e^{2L \times \frac{1}{2}(\Gamma g_{th} - \alpha_i)} = r_1 r_2 e^{(\Gamma g_{th} - \alpha_i)L} = 1, \quad (2.11)$$

and from equation (2.11), the equation can be rearranged as:

$$G = \Gamma g_{th} = \alpha_i + \alpha_m, \quad (2.12)$$

$$\alpha_m = \frac{1}{L} \ln \left( \frac{1}{r_1 r_2} \right) = \frac{1}{L} \ln \left( \frac{1}{R} \right), \quad (2.13)$$

In these equations,  $\alpha_m$  is referred to as mirror loss, representing the light that exits the laser through the facets. The point at which lasing begins,  $\Gamma g_{th}$ , is denoted as  $G$  and defined as modal gain. Since the optical intensity after one round trip cannot be greater than the initial intensity, the modal gain cannot exceed  $G$ , and consequently, the carrier density in the active region cannot exceed  $N_{th}$ . This concept is well illustrated in Fig.2-6.

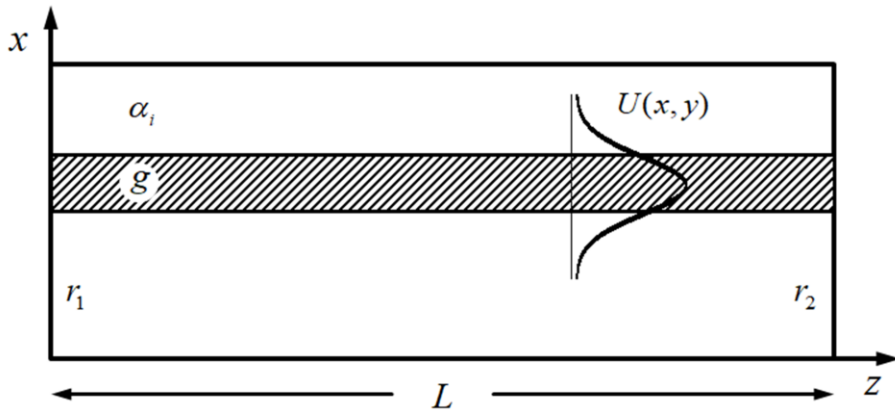


Fig.2-5. Generic cross-sectional schematic of laser cavity.



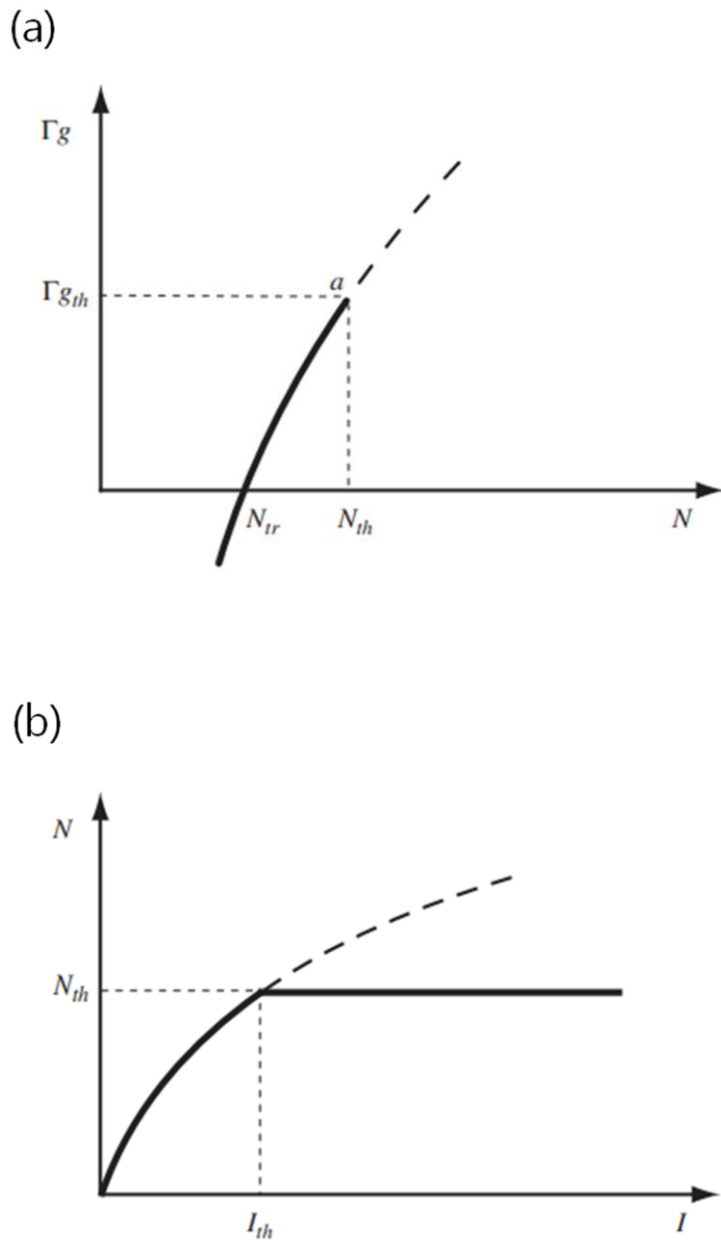


Fig.2-6. Material gain versus carrier density and carrier density versus input current [34].

### 2.3.2. L-I Characteristic

Semiconductor lasers are distinguished by the threshold current, which separates the dominant radiative recombination mechanism into spontaneous and stimulated recombination. Therefore, when analyzing the L-I (Light-Current) characteristics measured in a steady state, it's important to examine the region before and after the threshold current. Before reaching the threshold current,  $R_{st}$  can be considered to be nearly zero. Therefore, through (2.8), we can derive the following relationship for the steady state as:

$$\eta_i \frac{I_{th}}{qV_o} = \frac{N_{th}}{\tau}, \quad (2.14)$$

Through (2.14), the equation (2.8) after reaching the threshold current can be changed as:

$$\frac{dN}{dt} = \eta_i \frac{I}{qV_o} - \eta_i \frac{I_{th}}{qV_o} - v_g g_{th} N_p. \quad (2.15)$$

The stored optical energy in the cavity,  $P_{st}$ , is expressed as:

$$P_{st} = N_p h\nu V_p, \quad (2.16)$$

and using the concept of the energy loss rate through the mirrors,  $v_g \alpha_m$ ,

we can get the optical output power equation for the steady state as:

$$P_o = v_g \alpha_m N_p h\nu V_p = \eta_i \left( \frac{\alpha_m}{\alpha_i + \alpha_m} \right) \frac{h\nu}{q} (I - I_{th}), \quad (2.17)$$

## **2.4. Deep Learning Technique**

Deep learning is a subfield of machine learning that focuses on artificial neural networks (NNs), particularly deep neural networks (DNNs). Therefore, unlike general engineering simulations that calculate through lots of theoretical equations and iterations, deep learning is a simulation that predicts results given certain input values through various learning data. Therefore, if there is a well-trained DNN, it can reduce time and improve accuracy. The basic concepts of NNs are computational models inspired by the structure and functioning of human brain. NNs consist of layers of interconnected nodes, called neurons. Information flows through these networks with each neuron, and each time it passes through each neuron, a simple calculation is performed using weight and bias. DNNs are a kind of NN that has multiple hidden layers between the input and output layers. These multiple hidden layers enable DNNs to learn complex patterns and calculation from training data. A simple schematic structure of DNNs is shown in Fig.2-7. Research results in various engineering fields using deep learning are being reported [35-41].

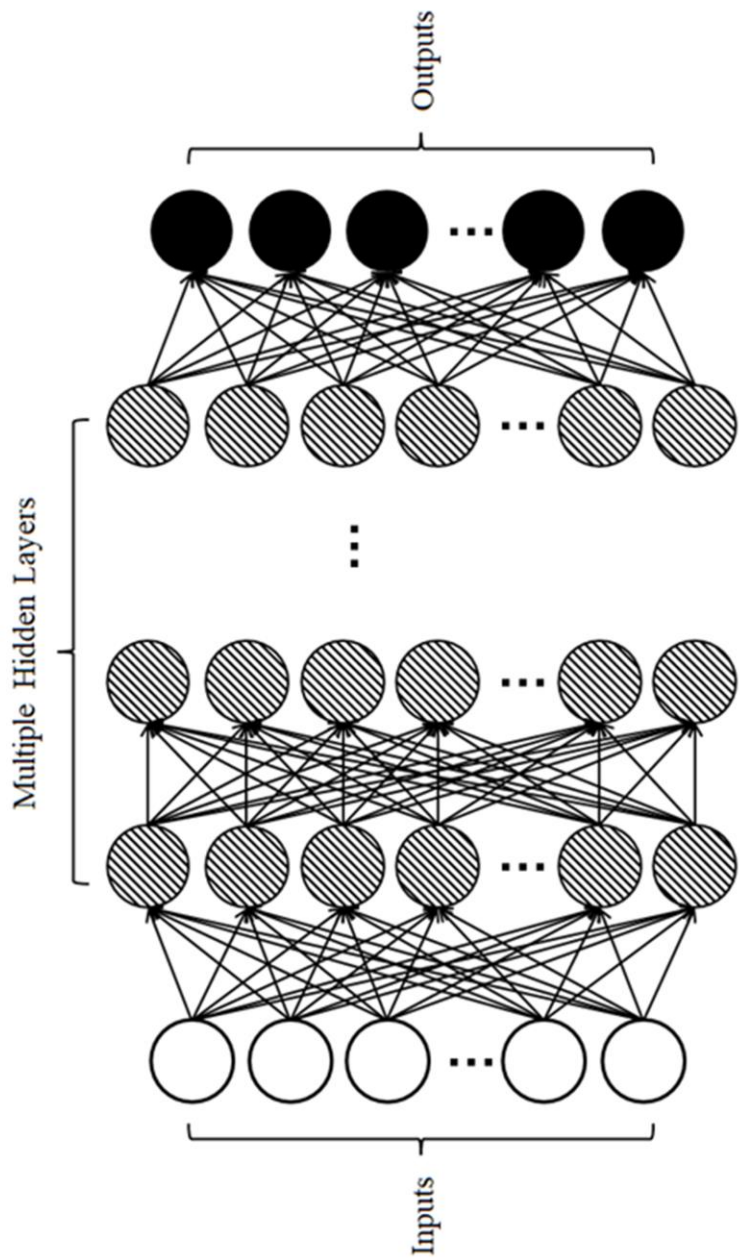


Fig.2-7. Simple schematic structure of DNNs.

### 2.4.1. Activation and Loss Function

Activation and loss functions are indeed essential for enabling neural networks to learn and accurately predict not only linear patterns but also nonlinear phenomena. When a DNN is trained, data is passed from one layer to the next through operations involving weights and biases at each neuron. Explaining data transfer without considering activation functions, when data moves from the  $k$ -th neuron in the  $(m-1)$ -th hidden layer to the  $n$ -th neuron in the  $m$ -th hidden layer, let's call each weight and bias as  $W_{(k,m,n)}$ ,  $b_{(k,m,n)}$  and the data at the  $n$ -th neuron in the  $m$ -th hidden layer as  $x_{(m,n)}$ . With this representation, if we consider the data  $x_{(0,1)}$  from the initial input passing through the first neuron in the first hidden layer and then the first neuron in the second hidden layer, the data at the end can be expressed as shown as:

$$x_{(2,1)} = W_{(1,2,1)} (W_{(1,1,1)} x_{(0,1)} + b_{(1,1,1)}) + b_{(1,2,1)}. \quad (2.18)$$

When you analyze this equation inductively, it ultimately results in a linear relationship with the input at the output, and consequently, it cannot properly learn nonlinear patterns. This implies that without the activation function, the neural network would essentially be a linear model, incapable of capturing and learning complex, nonlinear patterns in data. Activation functions are critical in introducing the necessary

nonlinearity into the network, enabling it to learn and represent a wide range of patterns and relationships. There are various types of activation functions, including sigmoid, ReLU, Tanh, Softmax, and in this study, ReLU was applied.

Loss functions, also known as a cost functions, are mathematical functions that measure the difference between the predicted values and the real values for a given set of input data. The choice of a loss function depends on the type of problem you want to predict and train for. For regression problems, Mean Squared Error (MSE) is typically used, while for classification problems, the cross-entropy function is applied. Additionally, users can create and use custom loss functions depending on the specific situation. MSE was applied in this study.

### **2.4.2. Training and Testing**

One of the significant advantages of DNNs compared to other machine learning methods is their ability to automatically achieve the best results. The process of training a DNN from start to finish occurs over multiple iterations, which are referred to as epochs. During these epochs, a DNN uses techniques like gradient descent and backpropagation to adjust its weights and biases automatically until it minimizes the loss calculated by the loss function during the training process. In order to conduct smooth gradient descent, the role of the optimizer is crucial. In this research, we used Adam.

Testing is the process of evaluating how well a well-trained DNN applies and generalizes to unlabeled data with input and output. When you have a large amount of data initially, you separate the data into training and testing sets. Then, for each epoch, you calculate the loss separately. The loss obtained during testing should generally be higher than what's obtained during training. However, as the number of epochs increases, the testing loss should also decrease, indicating that the DNN structure has learned properly.

### **3. High-Power Semiconductor Laser Structure for Improving Beam Quality**

High-power semiconductor lasers fundamentally require a large cavity for high output. As a result, they adopt a broad area structure with a wide stripe width and long cavity length. While this structure leads to the generation of numerous multi-modes, resulting in poor beam quality, its advantage lies in excellent Power Conversion Efficiency (PCE). Therefore, high-power semiconductor lasers are primarily used as pump light sources in laser systems that demand both high output and precision work. Light generated in semiconductor lasers is typically transmitted to other systems through fibers. Hence, improving beam quality, which determines fiber coupling efficiency, is crucial for energy transfer efficiency. Figure 3-1 illustrates the BPP of high-power semiconductor lasers reported in renowned international journals and conferences over the past decade [42-68], saturating at approximately 2-3 mm·mrad. While there have been studies on device structure and submounts [69-72] serving as heatsinks to enhance beam quality and address thermal issues, the most researched aspect is the suppression of far-field blooming caused by the enhanced thermal lensing effect at high power.



In this chapter, we introduce a pedestal structure that structurally enhances far-field blooming, which is a temperature-related issue. Building on this, we propose a double pedestal structure that improves beam quality and output power.

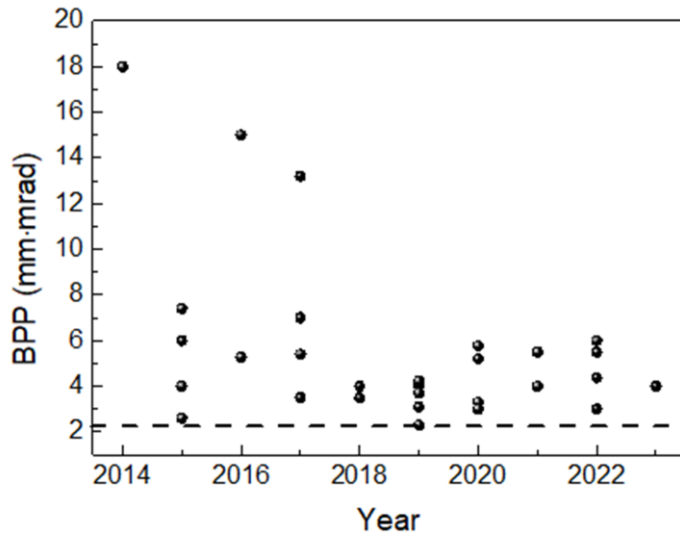


Fig.3-1. Reported results of BPP from international journals and conferences.

### **3.1. Far-Field Blooming**

In semiconductor lasers, optical waves in the active region are created at the center of the device through vertical and lateral waveguiding. Therefore, at high currents for high output, the temperature at the center of the device rises due to not only joule heat generated by carriers but also the high optical output. This induces temperature differences between the center and the edges and these temperature differences become more significant as the output power increases because semiconductor materials have the characteristic of increasing refractive index with temperature. It is leading to enhanced thermal lensing effect which strengthens lateral waveguiding [73-75]. This effect induces higher-order mode generation, which widens the overall far-field pattern, causing far-field blooming [74, 75]. These phenomena increase the divergence angle, consequently increasing the BPP and degrading beam quality.

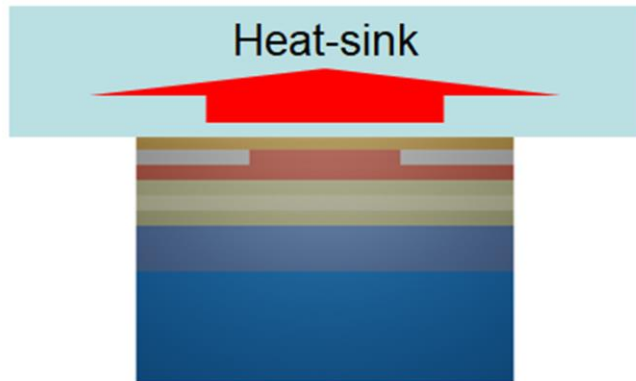
## 3.2. Pedestal Structure

To effectively suppress the far-field blooming caused by the persistent thermal lensing effect in high-power semiconductor lasers, it is crucial to design a heat dissipation structure that minimizes the temperature difference between the center and the edge of the component. A researched structure [76, 77] for this purpose involves utilizing a pedestal structure as a heatsink. Figure 3-2(a) schematically represents the typical heat dissipation structure of a semiconductor laser. Generally, it takes the form of a combination of a heat sink and the p-contact part of the component, allowing for the overall dissipation of heat from the component. In contrast, the pedestal heat-sink, illustrated in Figure 3-2(b), incorporates a pedestal structure between the heat sink and the component. This design facilitates the emission of a significant amount of heat from the center of the component. Using such a pedestal heat-sink structure helps reduce the temperature difference between the center and the edge of the component, thereby minimizing the thermal lensing effect. Additionally, it aids in suppressing the generation of high-order modes, which are a cause of far-field blooming.

Figure 3-3 presents simulation results before and after the use of the pedestal structure, as reported in reference [36]. Figures 3-3(a) and (b)

depict the L-I characteristics of higher-order modes as a function of the injected current for cases with and without the application of the pedestal heat-sink. When the pedestal structure is employed, a reduction in the occurrence of higher-order modes can be observed. Furthermore, in Figure 3-3(c), due to the suppression of higher-order mode generation, there is a decrease in the far-field angle, resulting in a decrease in the BPP and an improvement in beam quality. However, since the pedestal structure directs heat dissipation primarily towards the center, the overall heat dissipation is reduced. As a consequence, Figure 3-3(d) shows that the pedestal structure leads to a decrease in the maximum optical output.

(a)



(b)

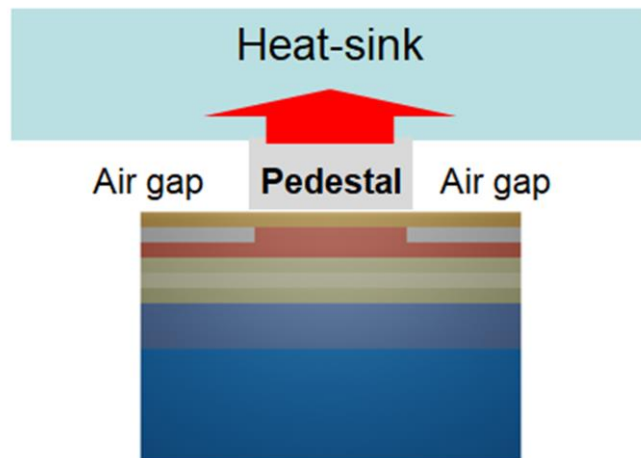


Fig.3-2. Schematic semiconductor laser structure including heatsink:  
(a) general type, (b) applying pedestal structure.

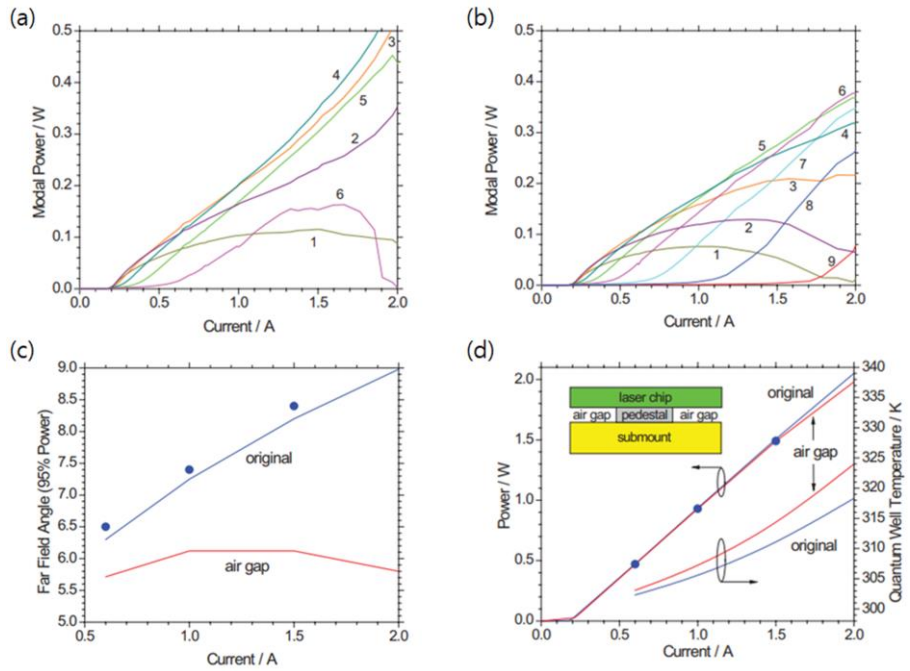


Fig.3-3. Calculated L-I characteristics of high-order modes with increasing current: (a) pedestal structure, (b) original structure, and (c) divergence angle of far-field pattern of original and pedestal structure, and (d) L-I characteristics and quantum well temperature of original and pedestal structure [77].

### **3.3. Double Pedestal Structure**

The heat-sink, responsible for dissipating heat in semiconductor lasers, is typically attached to the P-contact region. The reason for this is that attaching a heat-sink below the device, due to the thickness of the substrate being several hundred micrometers, does not significantly impact heat dissipation. However, if it were possible to eliminate the need for a thick substrate, attaching a heat-sink to the N-contact could have a meaningful effect. Drawing inspiration from the previously introduced pedestal structure, the double pedestal structure with upper and lower pedestal elements aims to enhance beam quality and increase output power through efficient heat dissipation from the center.

The component used in the research is a semiconductor laser with a wavelength of 852 nm, composed of GaInAsP, and it is a single quantum well component. It has a ridge structure with a cavity length of 2 mm and a stripe width of 100  $\mu\text{m}$ . The substrate is removed using the epitaxial lift-off (ELO) technique, and contact is established beneath through a pedestal structure. The analysis focuses on performance improvements based on the contact size.

### **3.3.1. Epitaxial Lift-Off Technique**

The Epitaxial Lift-Off (ELO) technique is a technology designed to reuse semiconductor substrates, aiming to reduce costs and enhance the manufacturing process. Initially, before growing the device, a sacrificial layer is epitaxially deposited on the substrate. The layers constituting the device are then grown on top of this sacrificial layer. Subsequently, the sacrificial layer is chemically removed, separating the substrate and the device. This enables the reuse of the substrate. The process for constructing a double pedestal structure follows the steps outlined in Figure 3-4. Figure 3-4 (a) illustrates the structure of a semiconductor laser utilizing a pedestal structure designed to dissipate heat only to the center through a ridge structure. Before growing the device, a sacrificial layer composed of AlAs is first grown on a GaAs substrate. The device is then constructed on top of this sacrificial layer. Subsequently, top metal bonding is performed as shown in Fig 3-4(b). Following this, as depicted in Fig. 3-4(c) and (d), the ELO technique is applied to separate the device from the GaAs substrate. Insulators and N-contact metal are then formed to create the bottom pedestal structure. Finally, in Fig. 3-4(e) and (f), heat sinks are attached to the bottom and top, forming a structure that efficiently dissipates heat to the center both from the top and bottom.



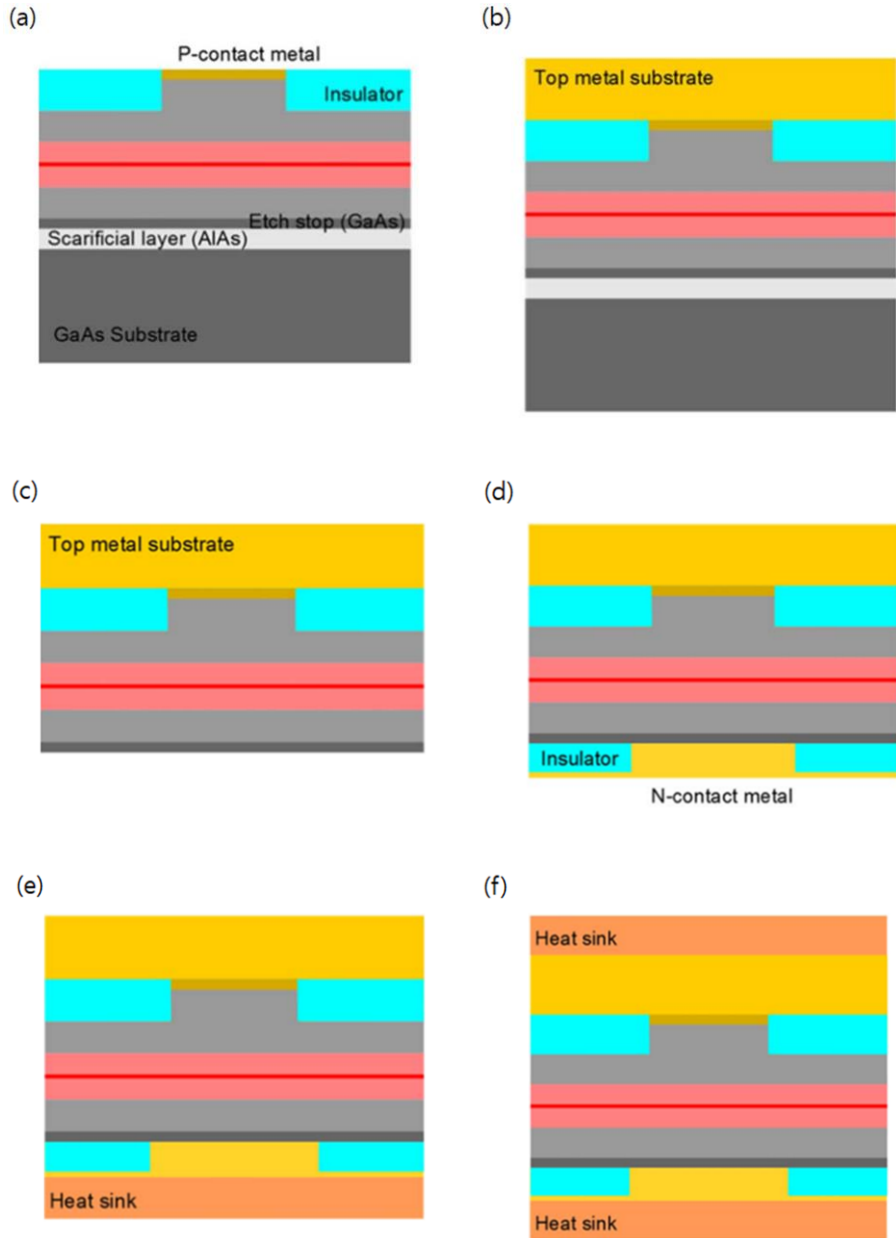


Fig.3-4. Fabrication process of DP structure with ELO technique: (a) semiconductor laser applying pedestal structure, (b) bonding of the top metal, (c) removal of substrate by ELO technique, (d) construction of the N-contact applying bottom pedestal structure, (e), (f) construction of bottom and top heat-sink [78].

### 3.3.2. Results

Figure 3-5(a) depicts a semiconductor laser employing the double pedestal structure produced through the previously introduced ELO technique. The simulation analyzes the changes in the L-I characteristics and far-field blooming as the size of the N-contact below varies (100, 140, 200, 400, 600  $\mu\text{m}$ ). Figure 3-5(b) represents the L-I characteristics and the maximum temperature in the quantum well with increasing current. As the contact size increases, the maximum optical output increases compared to the performance of the original device (Normal), and the temperature increase in the quantum well decreases. Figure 3-5(c) illustrates the temperature distribution in the x-direction, as indicated in Figure 3-5(a), at a current of 3 A. The results include the temperature distribution of the original device, the case with only the pedestal structure applied, and the results based on different contact sizes. When only the pedestal structure is applied, the overall temperature is higher than that of the original device due to heat dissipation only from the center of the component. However, a significant reduction in the temperature difference between the center and the edge is observed, leading to a decrease in the thermal lensing effect. Results with the double pedestal structure also show a pronounced reduction in the temperature difference between the center

and the edge, and overall, a decrease in the temperature of the quantum well. Figure 3-5(d) presents results for the half-divergence angle of the calculated far-field pattern and the maximum temperature in the quantum well at a current of 3 A. As the contact size increases, the heat dissipation increases, reducing the maximum temperature. However, the heat dissipation towards the center decreases relative to the edge, resulting in a decrease in the inhibitory effect on thermal lensing. Therefore, with increasing contact size, it is observed that the far-field angle increases.

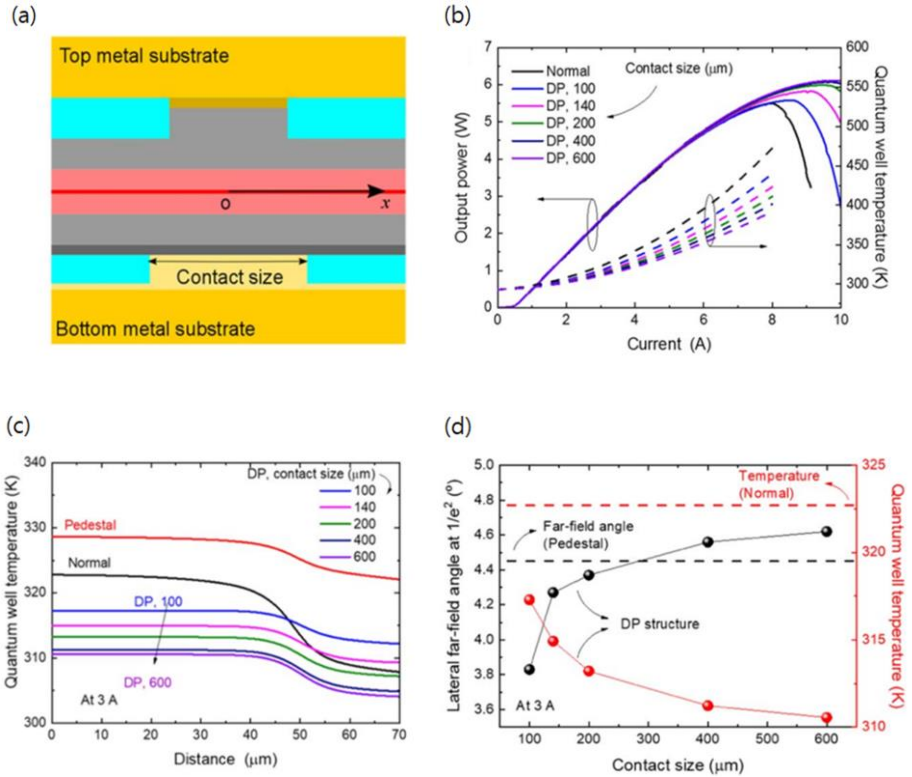


Fig.3-5. (a) Cross-sectional schematic of semiconductor laser applying double pedestal structure, and performance of the original device compared to the device with the application of pedestal and double pedestal structures: (b) L-I characteristics and quantum well temperature, (c) thermal distribution, and (d) divergence angle of far-field pattern of double pedestal structure with different contact size [78].

### **3.4. Summary**

In this chapter, we investigated a structure that could mitigate the far-field blooming, a temperature-related issue, in high-power semiconductor lasers. To suppress far-field blooming, our focus was on reducing the thermal lensing effect at high power. Drawing inspiration from the previously studied pedestal structure, we employed the ELO technique to separate the component from the substrate, forming a double pedestal structure both above and below to efficiently dissipate heat from the center. The double pedestal structure addressed the drawback of high quantum well temperatures in the pedestal structure, and its advantage of reducing the temperature difference between the center and the edge proved effective in mitigating thermal lensing and suppressing far-field blooming.

## 4. Single Mode Semiconductor Laser

As introduced in the previous chapter, the double pedestal structure, which suppresses far-field blooming occurring in high-power applications, has proven effective in improving beam quality. However, high-power semiconductor lasers with a broad area structure face limitations in enhancing beam quality due to the generation of multiple modes. For Gaussian beams with wavelengths between 850 and 970 nm, the BPP values are around 0.27 to 0.31, while high-power lasers exhibit values over ten times larger. Due to these limitations, there is renewed interest in the research of single-mode semiconductor lasers (SMSLs) that exhibit beam quality close to Gaussian beams. Unlike high-power semiconductor lasers, SMSLs have a narrow stripe width in the order of micrometers, resulting in fewer modes and an  $M^2$  value close to 1. Since it is challenging to separate and measure each mode, SMSLs are generally considered to have an  $M^2$  value between 1.1 and 1.5. Recent studies have been conducted to enhance the maximum output of SMSLs. Notably, TRUMF [79], a leading group in semiconductor laser development, reported the development of an SMSL of 930 nm with over 2 W output and  $M^2 < 1.5$ . They also developed an SMSL bar with over 200 W output, indicating the potential for high-power SMSLs to

serve as excellent pumping sources and, simultaneously, as direct optical sources for precision applications, rather than just as pumping sources. In the wavelength range of 9xx nm, semiconductor lasers are extensively researched as pumping sources for Yb-doped fiber lasers. However, in the 850 nm range, there is a limited amount of research or commercial devices operating as Single-Mode Semiconductor Lasers (SMSL) with power in the Watt range. Among the commercially available devices operating as SMSL in the 850 nm range provided by THORLABS, a leading company handling various optical devices, the device with the maximum output has a power of 600 mW [80]. Motivated by these considerations, we directly fabricated an 850 nm SMSLs with an output close to 1 W and an  $M^2$  value less than 1.5.

In this chapter, we analyze the L-I characteristics and far-field pattern of the actually fabricated 850 nm GaAs/AlGaAs SMSLs to evaluate beam quality. Additionally, we conduct an analysis of the observed non-linear phenomenon, the kink, through measurements.

## **4.1. Fabricated 850 nm GaAs/AlGaAs Single Quantum-Well SMSLs**

Figure 4-1(a) and (b) show cross-sectional views and SEM images of semiconductor lasers with a single quantum-well SMSL structure based on 850 nm GaAs/AlGaAs. Active region is composed of a 7nm quantum-well and barrier made of GaAs and AlGaAs, respectively. Vertical cladding is formed above and below the active layer through layers made of P-doped and N-doped AlGaAs. The ridge structure is formed through wet etching, and on both sides, a current block layer is designed to guide the current only to the center. The top (W) and bottom of the ridge are 2.4 and 4.6  $\mu\text{m}$ , respectively, and the SEM image of the device reveals its asymmetric structure. The cavity length (L) of the device is 1200, 1500, and 1800  $\mu\text{m}$ . Figure 4-2 represents the measured L-I characteristics, with threshold currents of 38, 43, and 53 mA and all devices have output optical power more than 600 mW. A prominent nonlinear feature known as "kink" is observed between 326-403, 394-497, and 479-551 mW of output power.



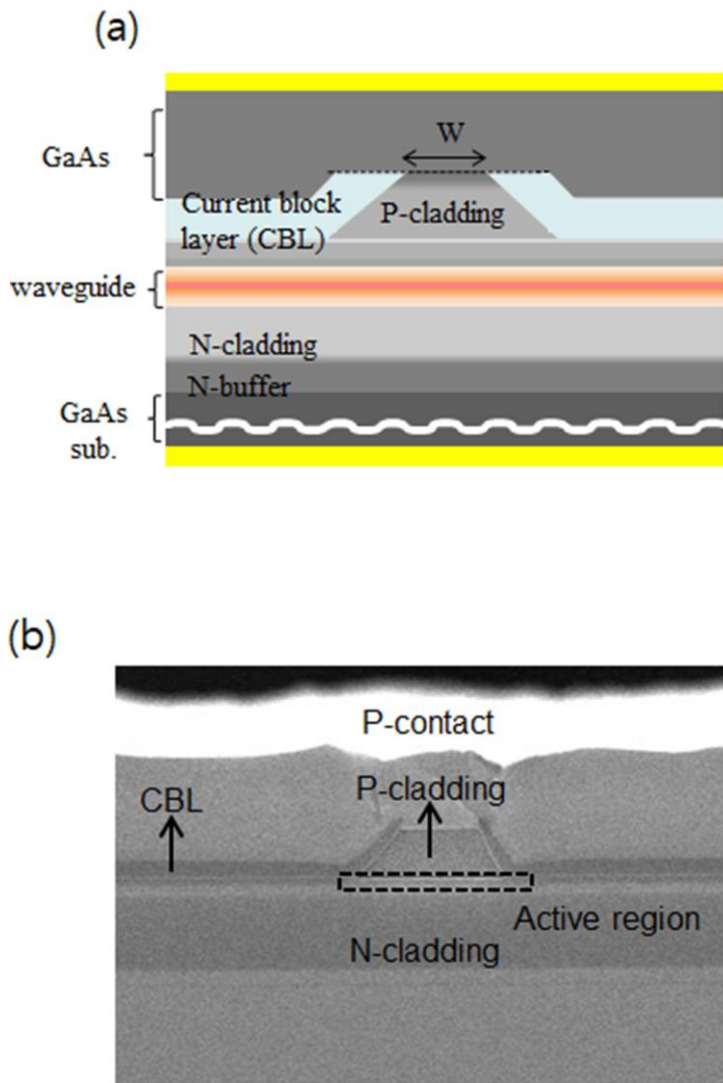


Fig.4-1. Fabricated single quantum well semiconductor laser based on GaAs/AlGaAs: (a) cross-section, (b) SEM image.

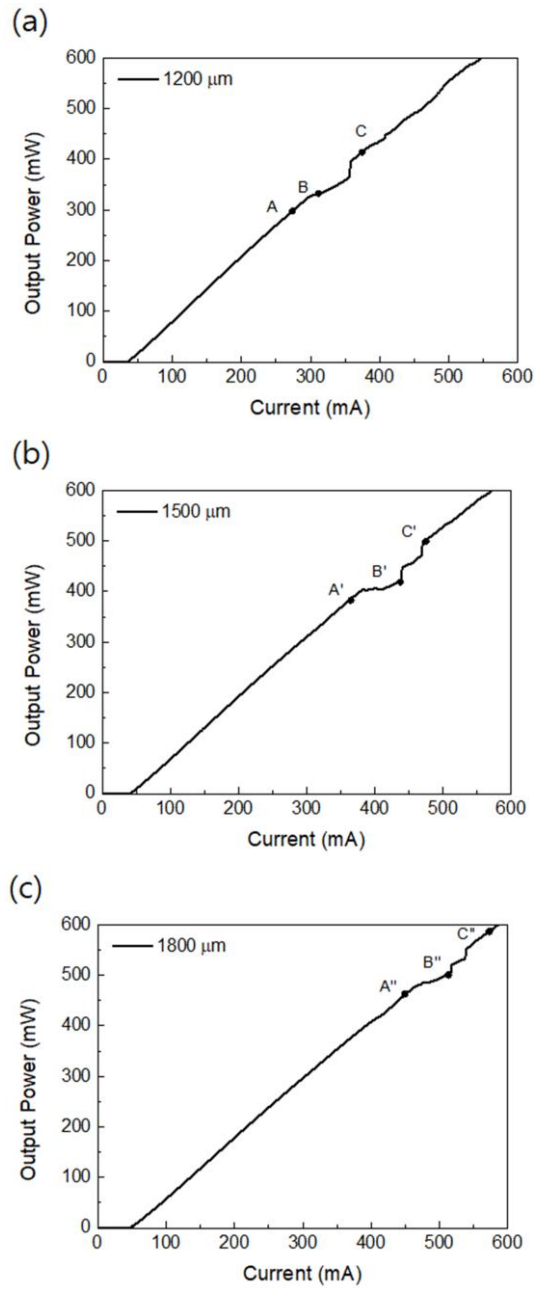


Fig.4-2. Measured L-I characteristics: (a)  $L = 1200$ , (b)  $1500$ , (c)  $1800 \mu\text{m}$ .

## 4.2. Kink and Far-Field Pattern Analysis

Theoretically, in semiconductor lasers, the multi-modes generated are considered as independent optical modes, and the calculated optical power in the L-I characteristics is obtained by summing the optical powers of each mode. However, in reality, interference between these modes occurs, leading to the observed kink. The exact point of mode interference that causes the kink is challenging to determine theoretically. Still, it is reported to result from the asymmetry in the fabricated device structure, which leads to an asymmetric effective refractive index [81, 82]. This mode interference causes the far-field pattern of the device to exhibit maximum intensity shifting from the center, resulting in beam steering and an asymmetric shape. As observed in SEM images of the studied devices, the asymmetric device structure is believed to be the cause of mode interference leading to the kink phenomenon.

Figure 4-3 illustrates the divergence angle concerning output power for  $L=1200, 1500,$  and  $1800 \mu\text{m}$ , demonstrating the presence of thermal lensing effect as output power increases. Figure 4-4 represents the far-field patterns in three scenarios: before the kink occurrence (A, A', and A''), after the kink occurrence (C, C', and C''), and within the region

where the kink occurred (B, B', and B''). In regions without kinks, the far-field pattern exhibits left-right symmetry. In contrast, in areas where the kink occurs, there's beam steering and asymmetric far-field pattern. This asymmetry indicates the interference between modes. To explore commonalities, additional analysis of the internal temperature of the device was conducted. Measuring the internal temperature of the device experimentally can be challenging. However, it can be indirectly inferred by observing the shift in resonance wavelength spectra at different temperatures.

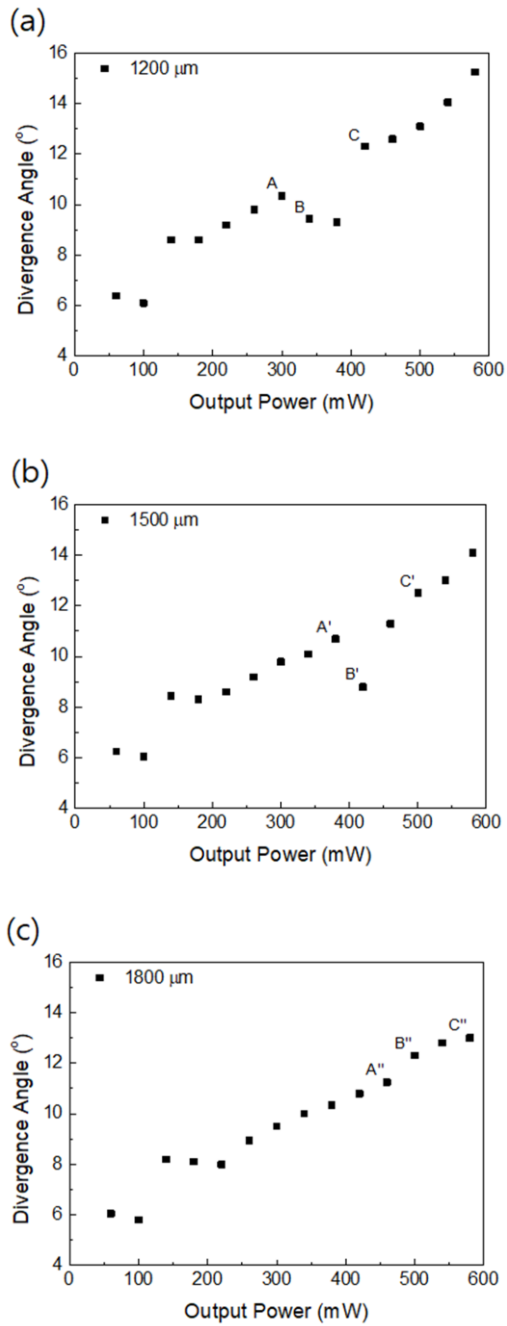


Fig.4-3. Measured divergence angles: (a)  $L = 1200$ , (b)  $1500$ , (c)  $1800 \mu\text{m}$ .

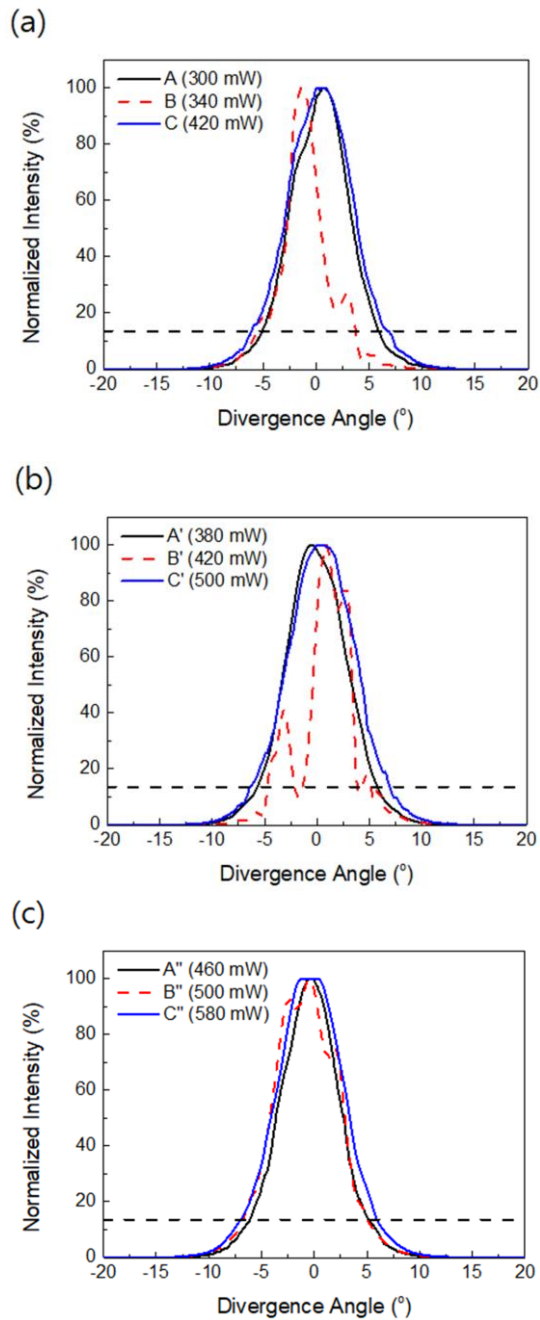


Fig.4-4. Measured far-field patterns in three scenarios: before the kink occurrence, after the kink occurrence, and within kink occurrence: (a)  $L = 1200$ , (b)  $1500$ , (c)  $1800 \mu\text{m}$ .

First, in Fig. 4-5(a)-(c), at an optical output power of 100 mW and environmental temperatures of 273, 293, 313, and 333 K, measured spectra show a linear resonance wavelength shift of 0.25 nm/K, as confirmed by Fig. 4-5(d). Next, measurements of the resonance wavelength were conducted for devices with cavity lengths  $L = 1200$ , 1500, and 1800  $\mu\text{m}$  at room temperature (295.5 K) across an optical power range of 60 to 580 mW with 40 mW intervals. These results are presented in Fig. 4-6(a)-(c). Using the relationship between temperature and resonance wavelength established earlier, it was possible to calculate the maximum internal temperature of the device. The calculated internal temperatures are also shown in Fig. 4-6(a)-(c), and it was observed that the range of temperatures where kinks occurred was consistent, ranging from 307 to 312 K.

The objective of the fabricated devices is to operate as SMSLs and achieve maximum output. Therefore, evaluations were conducted on a device with a  $L$  of 1800  $\mu\text{m}$ . The beam quality, measured through the divergence angle in Figure 4-3(c), indicates a BPP of 0.36 mm·mrad and an  $M^2$  value of 1.33 at 580 mW. Figure 4-7(a) presents data measured for the  $L=1800$   $\mu\text{m}$  component up to 750 mW, confirming its operation with powers exceeding 750 mW. Since the goal of device fabrication was to achieve power close to 1W, additional measurements

were conducted up to the Catastrophic Optical Damage (COD) level for a component with  $L=1200\ \mu\text{m}$ . The results, as shown in Figure 4-8(b), were measured at 700 mW. COD is influenced by the internal temperature and optical power of the device, and its level is proportional to the size of the cavity. Although not measured, it is anticipated that the  $L=1800\ \mu\text{m}$  device would have a COD level exceeding 1W.

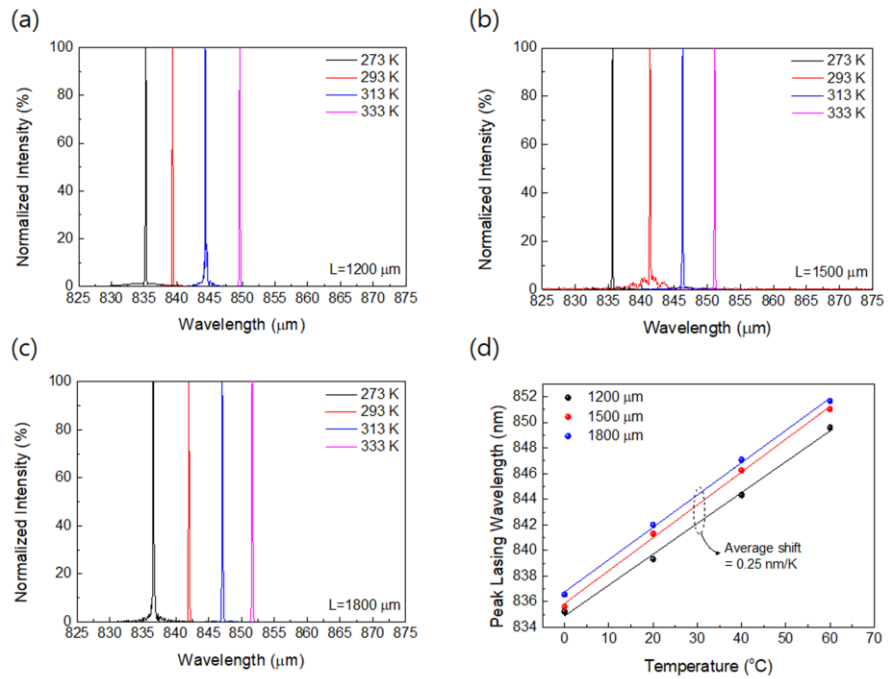


Fig.4-5. Measured resonance wavelengths of  $W=3\ \mu\text{m}$  at  $T=273, 293, 313, 333\ \text{K}$ : (a)  $L=1200$ , (b) 1500, (c) 1800  $\mu\text{m}$ , and (d) relationship between temperature and resonance wavelength.



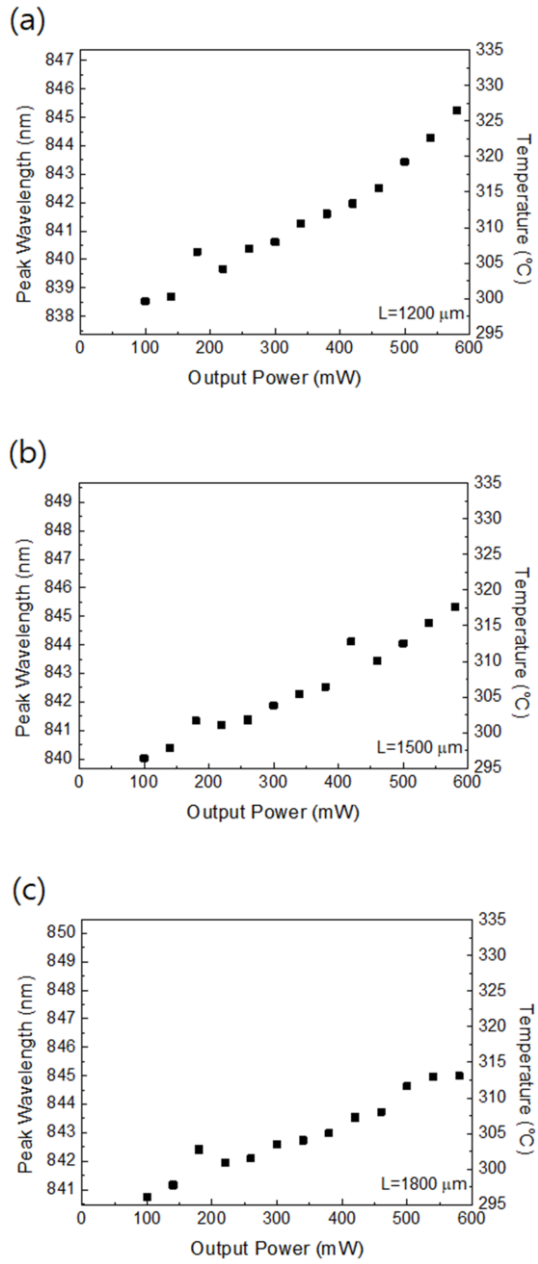


Fig.4-6. Measured resonance wavelength and calculated inner temperature of the devices: (a)  $L=1200$ , (b)  $1500$ , (c)  $1800\ \mu\text{m}$ .

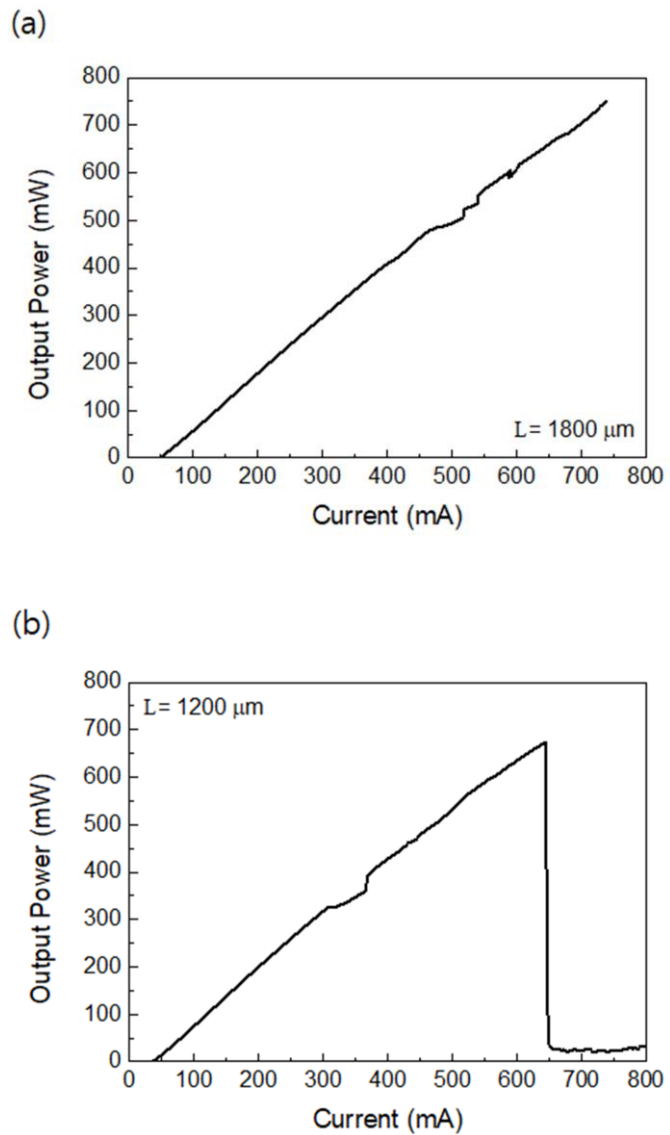


Fig.4-7. L-I characteristics: (a)  $L=1800 \mu\text{m}$  until 750 mW, (b) COD level of  $L=1200 \mu\text{m}$ .

### 4.3. Summary

In this chapter, we actually fabricated an 850 nm GaAs/AlGaAs-based SMSL due to the limitations in beam quality caused by the occurrence of multiple modes in high-power semiconductor lasers. we observed phenomena such as beam steering through the analysis of far-field patterns and spectra, investigating the kink observed in the L-I characteristics. Through this analysis, we identified mode interference causing the kink at specific temperatures. Additionally, the fabricated SMSLs demonstrated power levels exceeding 600 mW, showcasing performance surpassing the commercially available devices provided by THORLABS in the 850 nm range. For a device with a cavity length of 1800  $\mu\text{m}$ , we confirmed operation as an SMSL with over 750 mW and near 1 W optical output and an  $M^2$  value of 1.33 at 580 mW.

## 5. Optimizing Structure for Kink Suppression

In the previous chapter, an evaluation of beam quality was conducted on the fabricated 850 nm GaAs/AlGaAs single quantum-well device. However, due to the persistent occurrence of kinks, it was challenging to precisely assess beam quality. Additionally, in the fabrication process we use, wet etching is employed to create the ridge structure, leading to the formation of an asymmetric structure that causes kinking. Therefore, avoiding kinks in the produced SMSL is not straightforward. Hence, optimal structures that can suppress the occurrence of kinks by inhibiting the generation of the 1st order mode need to be optimized. Typically, for structural optimization, precise simulations are necessary. To achieve accurate simulations, it is crucial to accurately extract and model the design or key parameters that determine the performance of the device.

In this chapter, We propose a methodological approach to extract design parameters and perform structural optimization for precise simulations. We measure the design parameters and perform accurate extraction and modeling through deep learning. Utilizing these, we optimize structures through precise simulations to minimize the occurrence of kinks.

## **5.1. Design Parameters Extraction and Modeling**

In semiconductor lasers, one of the most critical metrics is the L-I (Light-Current) characteristic. This characteristic not only aims to enhance power conversion efficiency (PCE) to improve overall efficiency but also encompasses structural research focused on increasing output from single emitters [83-87]. Additionally, research in various forms such as modules, laser bars, stack packages, and more is actively underway to combine light emitted from multi-emitters to enhance optical output and beam quality [88-93]. When evaluating L-I characteristics, two major components are typically distinguished: threshold current and slope efficiency. These components are influenced by a combination of factors including structural information such as stripe width, cavity characteristics, layer structure, and doping details, which are essential for designing the device. Moreover, they are determined by material properties and process characteristics, including gain characteristics, internal loss, non-radiative recombination rates, and free carrier absorption (FCA). Typically, structural information is determined during the design and fabrication of the device, while parameters such as internal loss, non-radiative recombination rates, and FCA are influenced by the quality of the fabrication process. Hence,

these parameters are treated as design parameters for designing the device in a specific process. Internal loss can be experimentally measured and extracted by analyzing the L-I characteristics of devices with different cavity lengths, making it relatively straightforward [94-96]. However, non-radiative recombination coefficients and FCA coefficients are challenging to extract solely through experiments. They are typically considered as fitting parameters for simulation analysis [88, 97]. We aim to extract internal loss, Auger coefficient, and FCA coefficient as design parameters. We take advantage of the fact that SRH recombination has minimal influence on L-I characteristics. We introduce experimental measurement and temperature modeling for internal loss and propose using deep learning techniques, specifically a simple deep neural network (DNN), to extract and model the FCA coefficient and Auger coefficient, which were previously considered as fitting parameters.

### 5.1.1. Device Structure

Figure 5-1(a) illustrates the cross-sectional structure of the 850 nm GaAs/AlGaAs semiconductor laser used in this study. Layers, including three quantum wells (QWs) of double heterostructure, were grown on a GaAs substrate using the MOCVD technique. The laser was fabricated in a ridge waveguide form utilizing a current block layer (CBL). Each QW has a thickness of 8 nm, and, concerning the active region, it is sandwiched between the P-cladding layer above and the N-cladding layer below. The fabricated device has a stripe width ( $W$ ) of 1.4  $\mu\text{m}$ , and the reflectivity of the two facets composing the cavity is 0.11 and 0.95, respectively. The cavity length ( $L$ ) is 700  $\mu\text{m}$ . Figure 5-1(b) displays the L-I characteristics measured at experimental temperatures of 293 K, 303 K, 313 K, and 323 K. The threshold currents for these temperatures are 25 mA, 26 mA, 27 mA, and 28 mA, respectively.

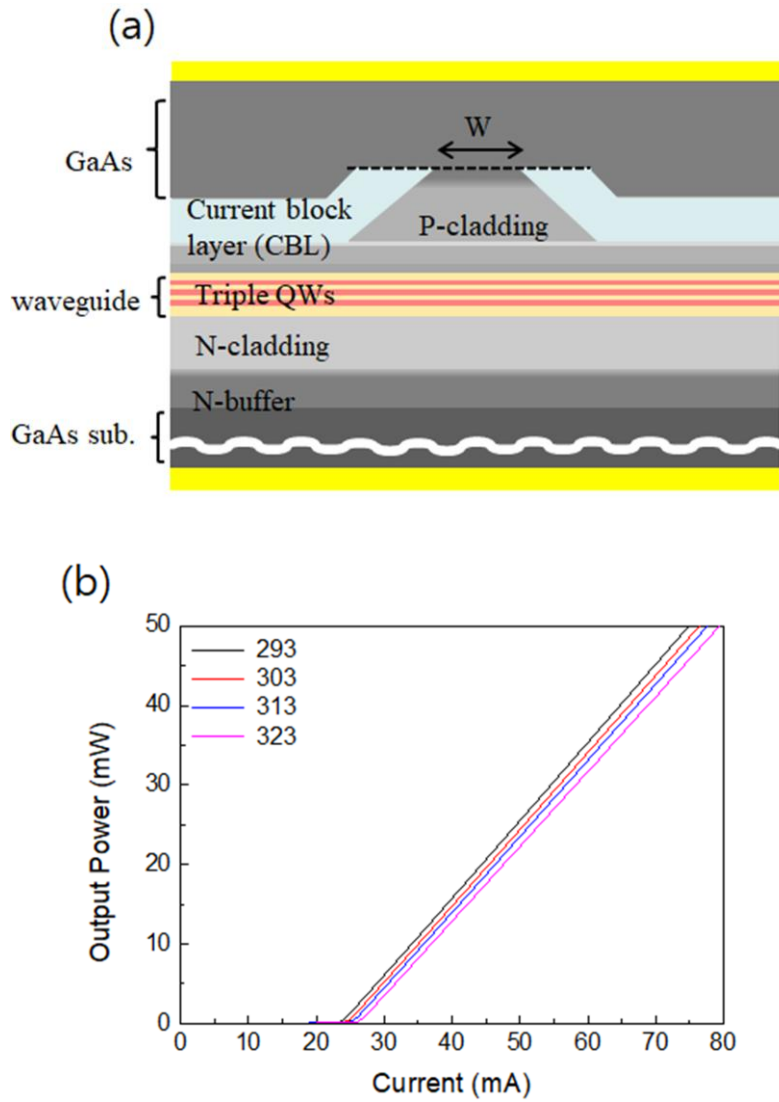


Fig.5-1. Fabricated 850 nm GaAs/AIGaAs multi-quantum well semiconductor laser: (a) cross-sectional structure and (b) L-I characteristics at 293, 303, 313, 323 K.



### 5.1.2. Internal Loss Modeling

The slope efficiency is defined as follows by the relationships derived in Chapter 2, specifically equation (2.13) for mirror loss and its relationship with cavity length, as well as equation (2.17) for the relationship between optical power and current,

$$\frac{dP_o}{dI} = \eta_d \frac{hw}{q} = \eta_i \frac{\frac{1}{L} \ln \frac{1}{R}}{\alpha_i + \frac{1}{L} \ln \frac{1}{R}} \frac{hw}{q}, \quad (5.1)$$

where  $\eta_d$  is expressed as

$$\eta_d = \eta_i \frac{\alpha_m}{\alpha_i + \alpha_m}. \quad (5.2)$$

By rearranging the (5.2) in terms of  $1/\eta_d$  using (5.1), we can obtain a linear relationship with respect to  $L$ .

$$\frac{1}{\eta_d} = \frac{1}{\eta_i} + \frac{1}{\eta_i} \frac{\alpha_i}{\ln\left(\frac{1}{R}\right)} L. \quad (5.3)$$

Based on the information provided,  $L$  and  $R$  values are known, but the unknown variables to be extracted are  $\alpha_i$  and  $\eta_i$ . To determine these values, components with  $L$  values of 300 and 1100 have been fabricated. The experimentally measured slope efficiency for these components with  $L$  values of 300, 700, and 1100  $\mu\text{m}$  at temperatures of 293, 303, 313, and 323 K is used to calculate  $1/\eta_d$ . The results for  $1/\eta_d$  are represented by symbols and curves in Fig.5-

2(a). The curves measured in Fig.5-2(a) confirm linearity with cavity length as shown in (5.1), and by obtaining the y-intercept from the linear fit,  $\eta_i$  can be calculated. Additionally,  $\alpha_i$  can be calculated using the slope of the line and  $\eta_i$ . The values of  $\alpha_i$  calculated for each temperature are shown in Fig.5-2(b). Furthermore, it can be observed that it linearly increases with temperature. The thermal modeling obtained from Figure 5-2(b) is expressed as:

$$\alpha_i(T) = \alpha_o + \beta(T - 298), \quad (5.4)$$

where  $\alpha_o$  is the internal loss at 298 K and  $\beta$  is rate of the increase in internal loss with temperature. In this device, each extracted value of  $\alpha_o$  and  $\beta$  is  $12.18 \text{ cm}^{-1}$  and  $0.041 \text{ cm}^{-1}/\text{K}$ .

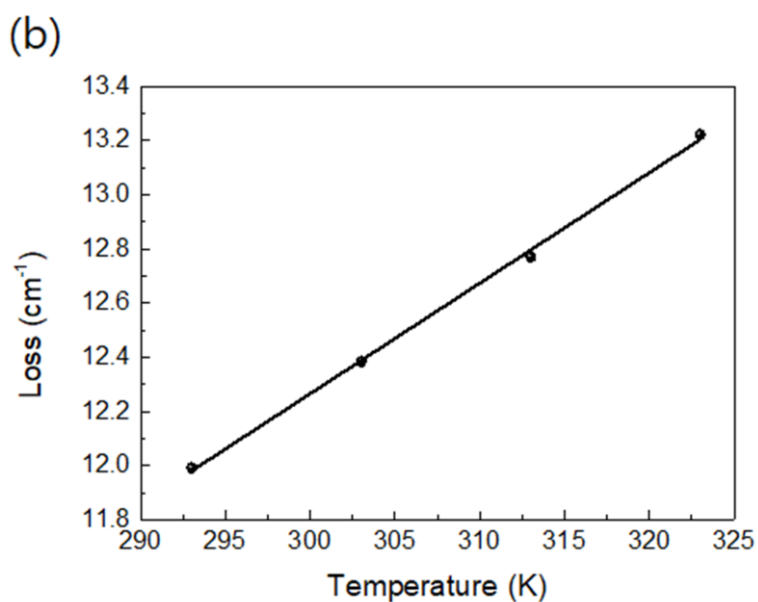
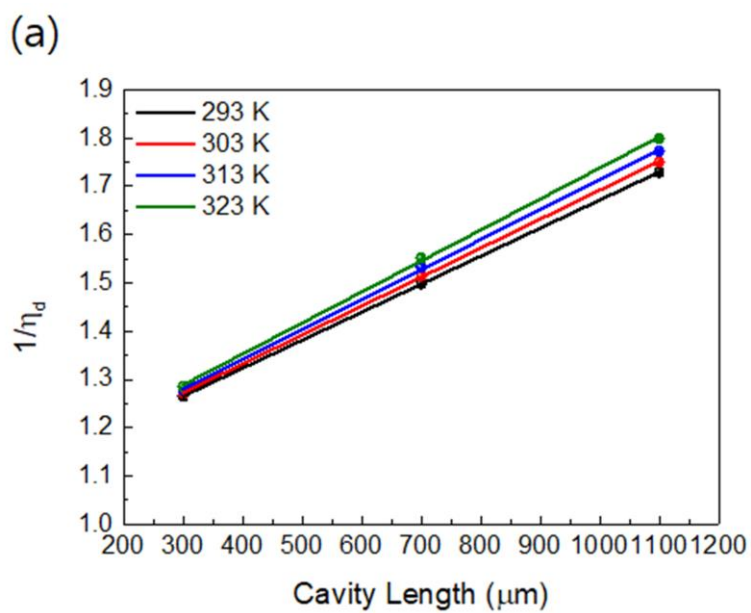


Fig.5-2. (a) Measured  $1/\eta_d$  versus  $L = 300, 700, 1100 \mu\text{m}$  and (b) extracted internal loss versus temperature at 293, 303, 313, 323 K.

### **5.1.3. Auger and FCA Coefficients Modeling Based on DNNs**

Deep learning techniques have become a powerful tool not only for analyzing linear relationships between causes and effects or inputs and outputs, as introduced in Chapter 2.4, but also for analyzing nonlinear relationships. As a result, research incorporating deep learning is being reported in various optical fields, including optical communication [98, 99], image reconstruction [100, 101], and the inverse design of optical devices [102, 103]. Additionally, research has been reported in which a simple neural network structure called a deep neural network (DNN) was used for the inverse design of semiconductor lasers' design parameters [104, 105]. In [104], seven design parameters such as injection efficiency, heat capacity, series thermal resistance, device temperature, gain characteristic, carrier characteristic and loss that determine the L-I characteristics of a semiconductor laser were set as inputs, and 60 optical powers at different currents were set as outputs. A DNN was trained to mimic the L-I characteristic simulation. The data used for training and testing were generated from a laser simulation based on the TWM (Traveling wave model). The results showed a good match between the L-I characteristics obtained from the trained DNN and those obtained from the laser simulation. The well-trained DNN

can be used in combination with the Particle Swarm Optimization (PSO) algorithm to extract the seven design parameters required to achieve the desired L-I characteristics, as explained. The research results demonstrate the potential of inverse design for semiconductor lasers by extracting multiple sets of parameter values. However, it's important to note that this approach may introduce significant uncertainty from a material property perspective, as specific materials and fabrication often require precise parameter values. Therefore, in this chapter, we aim to extract our designated design parameters one by one through experimentation and simulation for accuracy.

#### **5.1.4. Algorithm and DNN Structure**

In the case of Auger and FCA coefficients, they are not easy to experimentally extract and model independently, similar to internal loss. Therefore, their values are determined through numerous trial-and-error iterations by comparing simulated and measured L-I characteristics. In this research, we applied deep learning to eliminate human-dependent trial-and-error processes, aiming for consistency and precision in parameter extraction. Figure 5-3 and 5-4 illustrate the consecutive DNN structure and overall process used in our study. As mentioned earlier, we will be extracting and modeling the Auger and FCA coefficients one by one, labeled as #DNN1 and #DNN2 in the structure. Each DNN consists of three inputs, one output, and three hidden layers, each containing 512 elements. When distinguishing the L-I characteristic into threshold current and slope efficiency regions, the threshold current is determined by losses and the Auger coefficient [96, 105]. On the other hand, slope efficiency is determined by internal loss, the Auger coefficient, and the FCA coefficient [96]. Therefore, for #DNN1, which outputs the Auger coefficient, the inputs include experimentally obtained environmental temperature and the threshold current of the device, as well as the measured internal loss. For #DNN2, which outputs the FCA coefficient, the inputs include the

experimentally obtained slope efficiency and internal loss, as well as the Auger coefficient extracted from #DNN1. In the DNN, the Mean Squared Error (MSE) was used as the loss function, and the Adam optimizer was employed. ReLU activation functions were used as well. To ensure that the DNN was well-trained, it was trained for a million epochs.

Generating the required training dataset involves conducting L-I characteristic simulations while varying the values of internal loss  $[\alpha_0, \dots, \alpha_{h-1}]$ , the Auger coefficient  $[C_0, \dots, C_{j-1}]$ , the FCA coefficient  $[k_0, \dots, k_{m-1}]$ , and temperature  $[T_0, \dots, T_{n-1}]$ . Properly preparing the data is essential for the effective training of the DNNs. In the case of DNN#1, where the FCA coefficient has a limited impact on the threshold current, simulations are carried out with  $k_0 = 0$ . In the case of DNN#2, simulations are conducted at a specific temperature ( $T_s$ ), assuming no temperature dependence in the FCA coefficient. This strategic approach reduces the number of required simulations from  $(h \times j \times m \times n)$  to  $(h \times j \times n) + (h \times j \times m) - (h \times j)$ . Following this, the generated data is divided into training and testing sets. Given that the performance of the DNNs is affected by the quality of the training data, it is crucial to identify the DNN with the lowest testing loss. To accomplish this, the process of "Finding appropriate DNN#1" in Fig.5-

4 is necessary. The training and testing datasets are selected by iteratively changing the testing set, similar to cross-validation. After training is conducted for each iteration, the training and testing datasets with the lowest testing loss are chosen for DNN training. To illustrate DNN#1, in Fig.5-5, let's consider it based on the output Auger coefficient. It can be divided into  $j$  datasets, each containing  $h \times n$  data points from  $C_0$  to  $C_{j-1}$ . For smooth training, the first and last datasets must be included in the training dataset. Therefore, the testing dataset can have its Auger coefficient set to any value from  $C_1$  to  $C_{j-2}$ . By iteratively changing the Auger coefficient in the testing dataset through  $j-2$  iterations, the testing dataset with the lowest testing loss is selected. DNN#1 is then applied to extract the Auger coefficient from this selected testing dataset. The deep learning implementation utilizes open-source Python and PyTorch libraries.



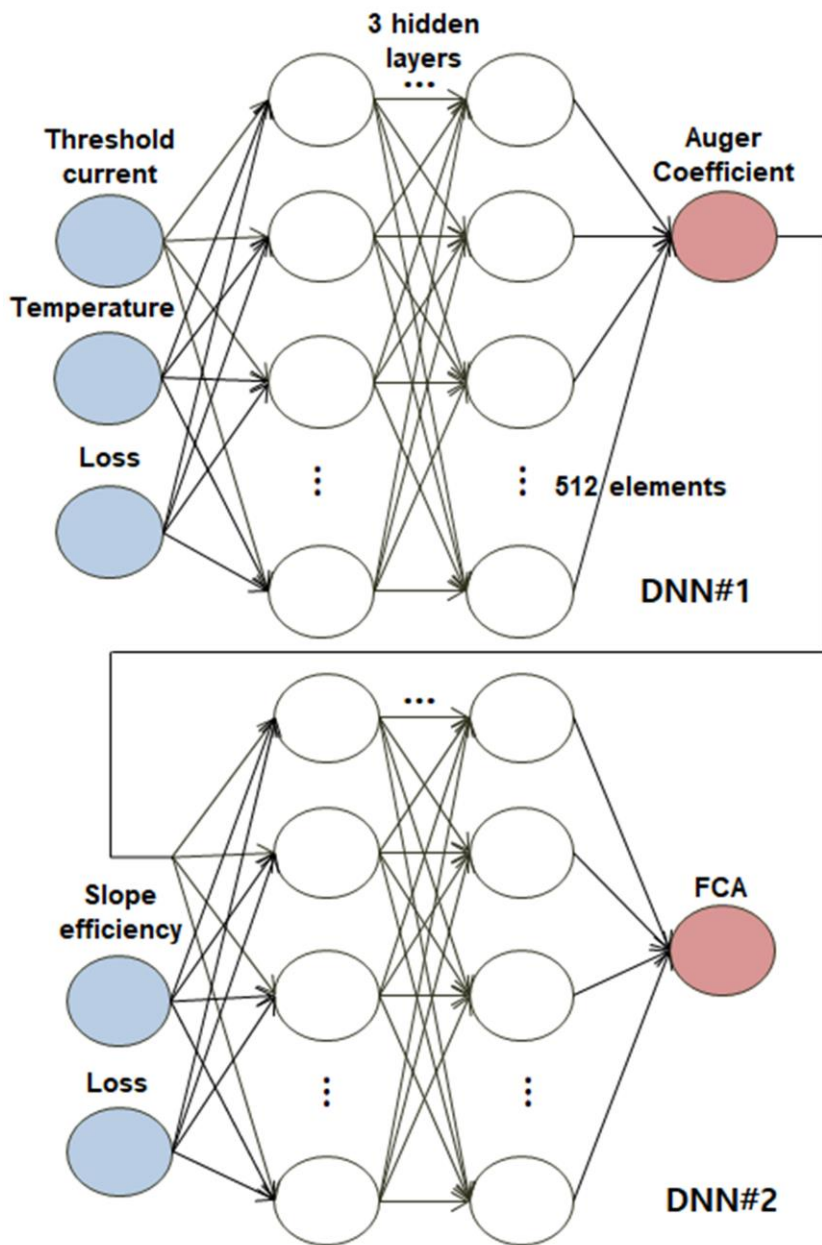


Fig.5-3. Consecutive schematic structure of DNN.

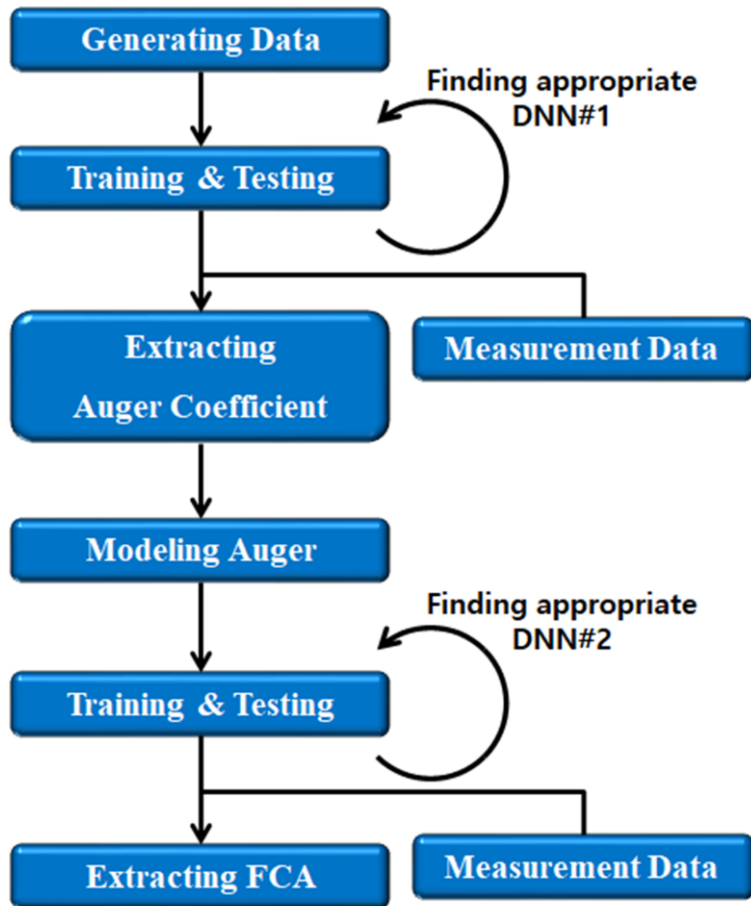


Fig.5-4. Overall process of parameter extraction.

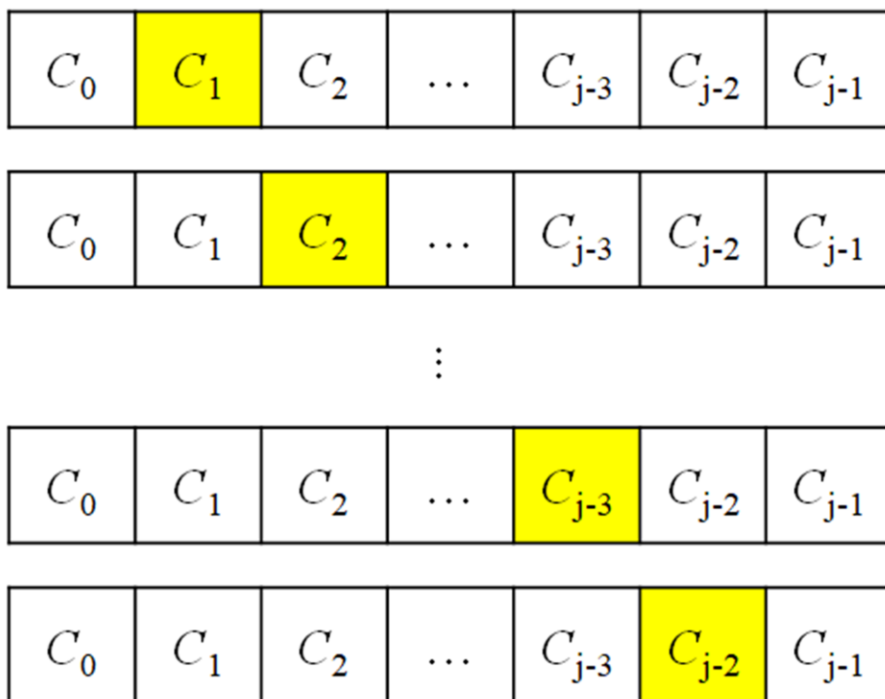


Fig.5-5. Process of iteration for finding testing dataset which has minimum testing loss.

### 5.1.5. Results

A total of 448 L-I characteristic simulation was conducted, covering various parameter values. This encompasses internal loss values ranging from [1, 3, 5, 7, 9, 11, 13, 15]  $\text{cm}^{-1}$ , Auger coefficients ( $C$ ) spanning [0, 1, 3, 5, 7, 9, 11]  $\times 10^{-30} \text{cm}^6\text{s}^{-1}$ , and FCA ( $k$ ) values from [0, 1, 2, 3, 4]  $\times 10^{-18} \text{cm}^{-2}$ , all assessed at different temperatures of [293, 303, 313, 323] K. Figure 5-6(a) and (b) display the training and testing loss curves of DNN#1 when the testing set's  $C$  values are [1, 3, 7, 9]  $\times 10^{-30} \text{cm}^6\text{s}^{-1}$ . Notably, the absence of a curve for  $C_3 = 5 \times 10^{-30} \text{cm}^6\text{s}^{-1}$  is due to the lack of training data. While the training loss curves suggest well-trained DNNs for all cases, Figure 5-6(b) highlights that the testing set with  $C_1 = 10^{-30} \text{cm}^6\text{s}^{-1}$  is unsuitable for DNN#1. Consequently, the appropriate DNN#1 is determined to be the one aligned with the testing set of  $C_4 = 7 \times 10^{-30} \text{cm}^6\text{s}^{-1}$ , exhibiting the minimum loss.

Leveraging DNN#1, Auger coefficients of the device are extracted at various temperatures, as depicted in Fig. 3-6. Using a well-established model equation represented as [27]:

$$C(T) = C_o \exp\left(\frac{E_a}{k_{\text{Boltzmann}} T}\right), \quad (3.5)$$

where  $E_a$  is the activation energy and  $k_{\text{Boltzmann}}$  is the Boltzmann

constant, we obtain extracted values of  $C_o$  equal to  $3.95 \times 10^{-27}$   $\text{cm}^6\text{s}^{-1}$  and  $E_a$  equal to 167.5 meV. The corresponding modeling curve is presented in Fig. 5-7, and this extracted Auger model automatically becomes an input for DNN#2.

Figure 5-8(a) and (b) display the training and testing curves of DNN#2 at  $T_1 = 303$  K when the testing set's  $k$  values are  $[1, 2, 3] \times 10^{-18} \text{ cm}^{-2}$ . The absence of a curve for  $k_3 = 3 \times 10^{-18} \text{ cm}^{-2}$  is due to insufficient training data. Notably, the suitable DNN#2 is found for the testing set aligned with  $k_2 = 2 \times 10^{-18} \text{ cm}^{-2}$ , as shown in Fig. 5-8(b). Consequently, the extracted FCA coefficient is determined to be  $1.01 \times 10^{-18} \text{ cm}^{-2}$ .

Finally, a verification process is conducted to validate the accuracy of the extracted values. The L-I characteristics are recalculated using the extracted parameters across various temperatures. The simulation results and the measured data are compared in Fig. 5-9 at different temperatures, showing a close alignment between the two.

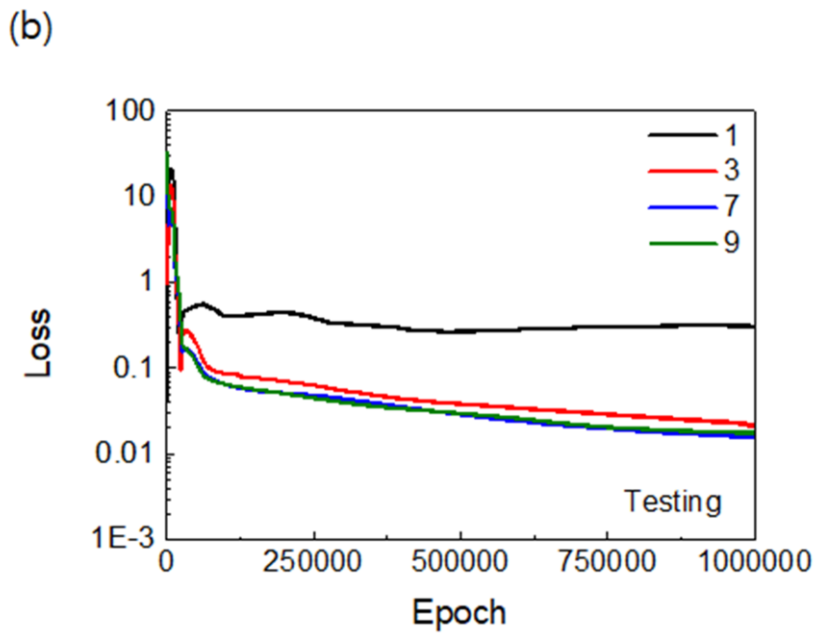
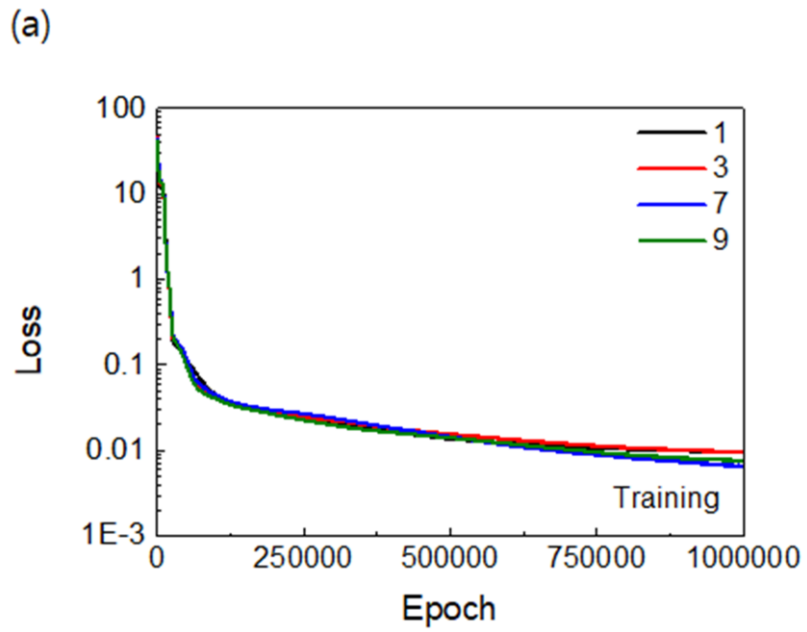


Fig.5-6. Loss curves of DNN#1 of (a) training and (b) testing.

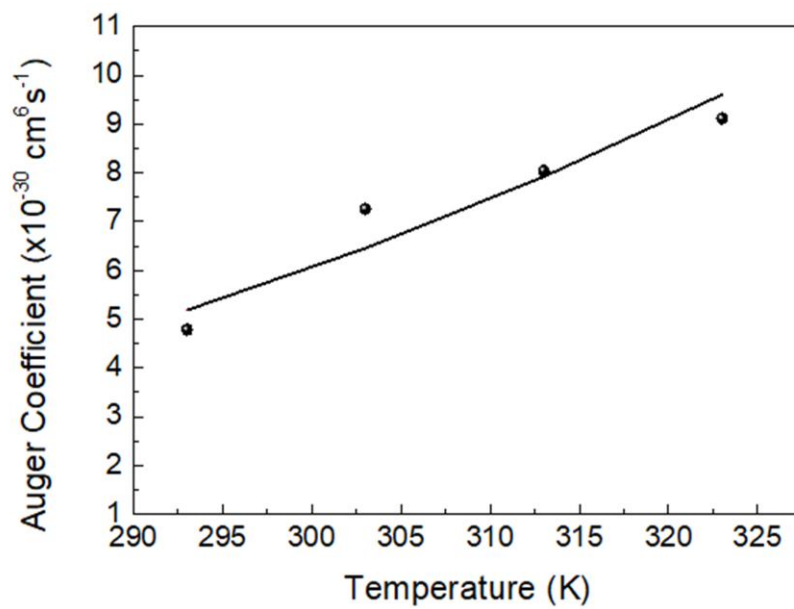


Fig.5-7. Extracted values and curve of Auger coefficient.

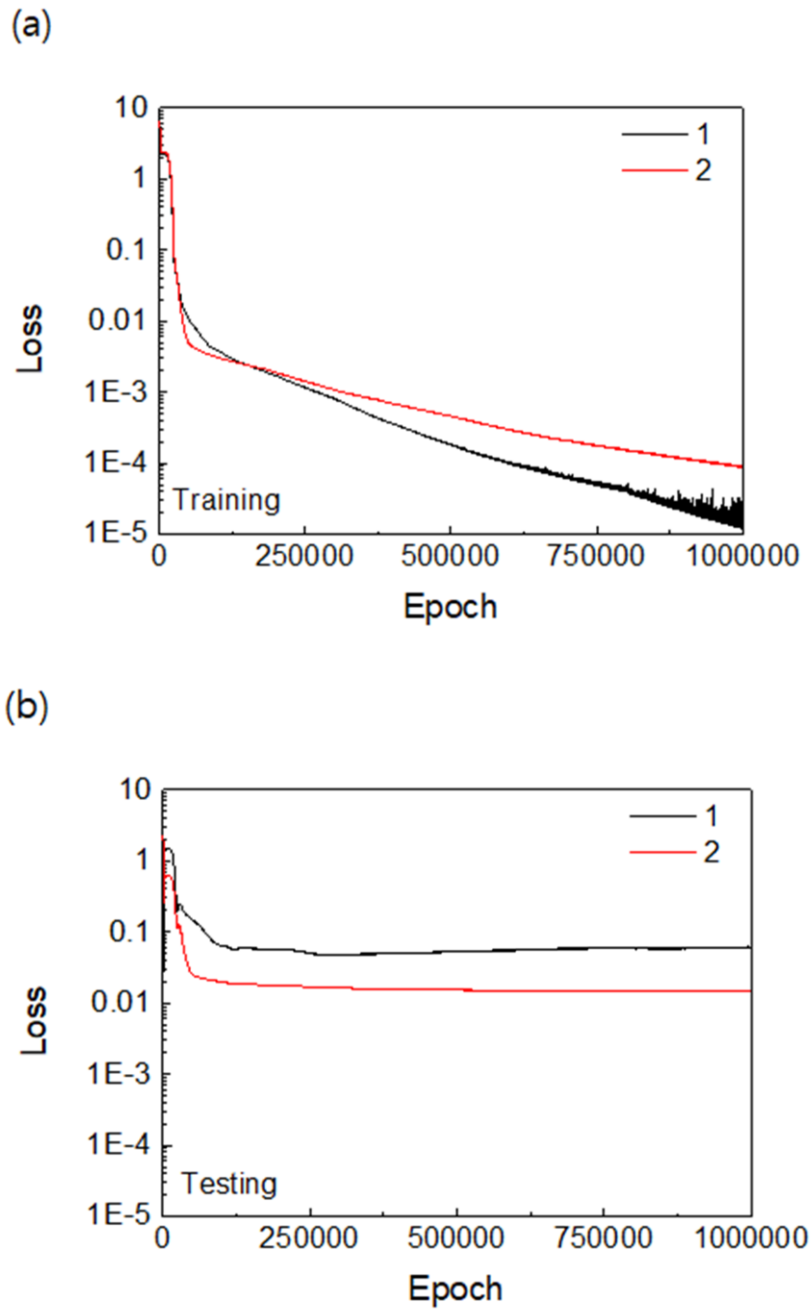


Fig.5-8. Loss curves of DNN#2 of (a) training and (b) testing.



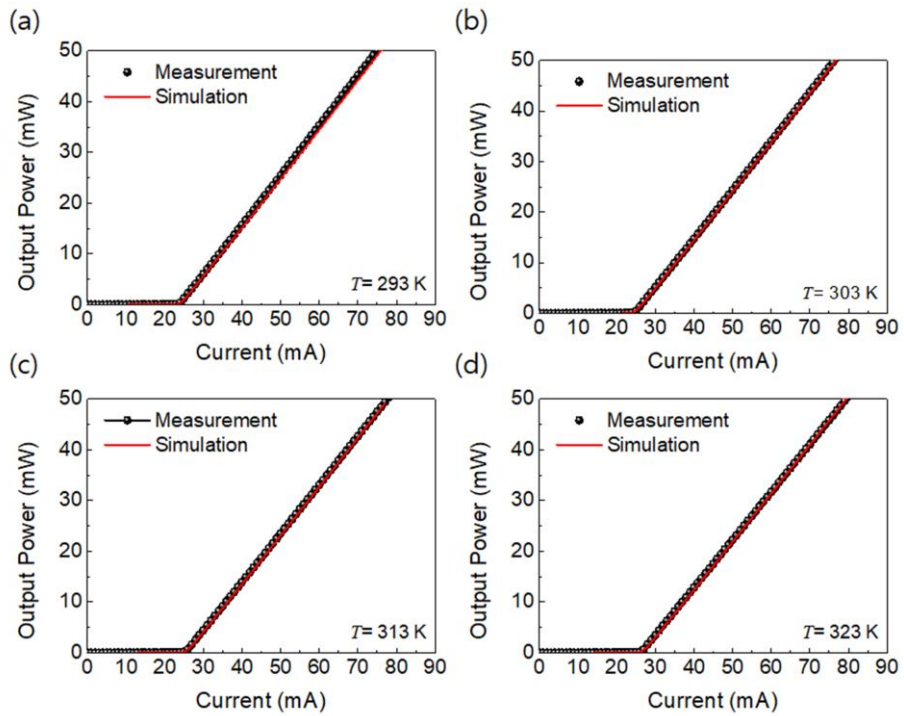


Fig.5-9. L-I characteristics of simulation and measurement at (a) 293, (b) 303, (c) 313 and (d) 323 K using extracted parameters.

## 5.2. Simulation Validation of $W=3\ \mu\text{m}$

In addition to further validating the accuracy of the simulation composed of the extracted and modeled parameters, we fabricated a device with  $W=3\mu\text{m}$  to increase the maximum output of the device. Figure 5-10 presents both measured and simulated L-I characteristics, where kink becomes prominent in the power range of 60 to 160 mW. Fortunately, the simulation results match well with the measured data. Regrettably, our simulation tool does not account for nonlinear phenomena such as kinking. Therefore, further validation is required for the discrepancy between the measured values and simulations in the linear-looking range of 75 to 150 mW. The inserted images in Fig 5-10 depict the far-field patterns at 120 mW and 220 mW optical output. At 120 mW, beam steering and asymmetric far-field patterns are observed, indicating mode interference and a reduction in optical power. Conversely, at 220 mW, where simulation and measurement values overlap, a symmetric far-field pattern with no beam steering is observed, confirming the absence of mode interference. The analysis of these two far-field patterns further reinforces the reliability of the L-I characteristic simulations. Additionally, through the simulation, it can be confirmed that the 1<sup>st</sup> order mode is generated at around 60 mW. To

validate the simulation results, the divergence angle was measured for various optical powers, and the results are shown in Figure 5-11(a). The measurement results revealed a sharp increase in the divergence angle at 60 mW, indicating the emergence of new higher-order modes. Figure 5-11(b) compares the measured far-field patterns at 40 and 60 mW with the simulated far-field pattern at 40 mW, showing a good agreement between the measurement and simulation results. Based on this, the calculated BPP and  $M^2$  values at 40 mW were 0.27 and 1, respectively, indicating the presence of only the fundamental mode at 40 mW. Taking these results into consideration, it can be confirmed that around 60 mW, the 1<sup>st</sup> order mode is observed in the actual device, consistent with the simulation results.

Furthermore, it's necessary to verify whether the thermal calculations performed in the simulation tool are accurate. Figure 5-12(a) shows the resonance wavelength spectrum measured at temperatures of 283, 303, and 323 K, confirming a wavelength shift of 0.1725 nm/K due to temperature variations. As analyzed in the SQ device, the measured resonance wavelength, up to 340 mW optical power, and the calculated internal temperature of the device are presented in Fig.5-12(b). The internal temperature calculated through simulation is represented by the solid line. These all results collectively

validate that the simulation accurately replicates the performance of the device.

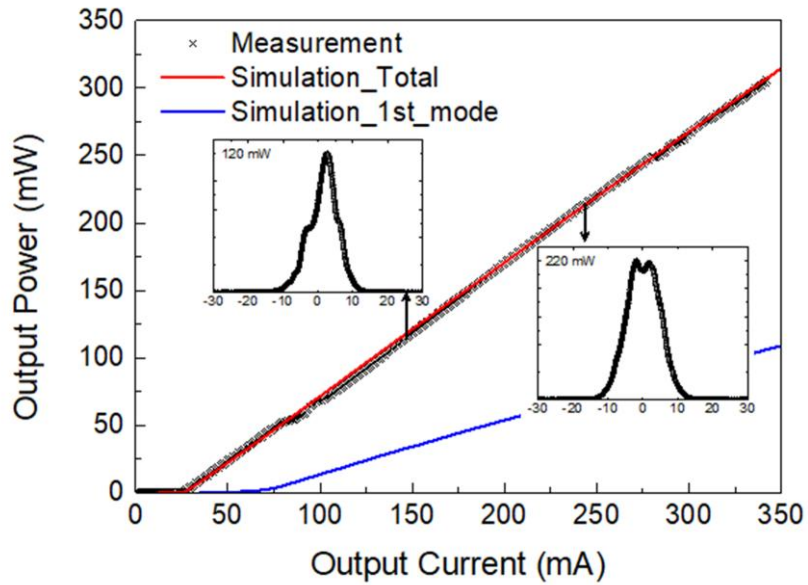


Fig.5-10. Fabricated 850 nm GaAs/AlGaAs multi-quantum well semiconductor laser of  $W=3\ \mu\text{m}$ : Measured L-I characteristic and insets of far-field pattern at 120 and 220 mW.

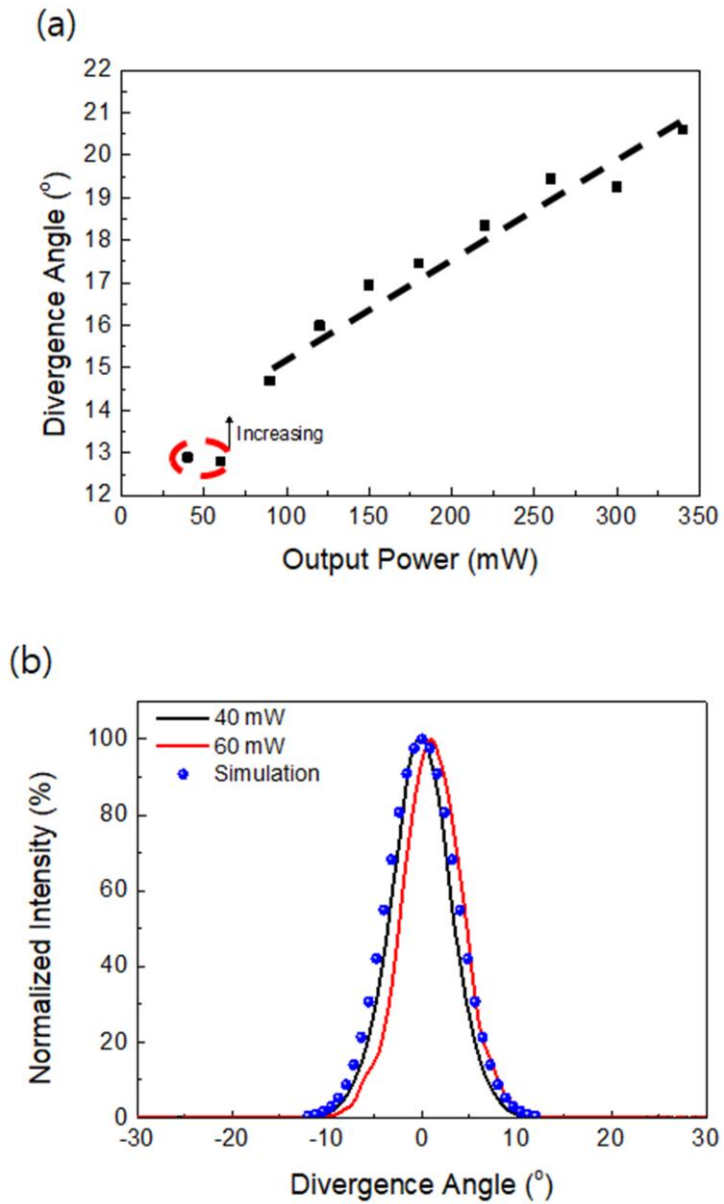


Fig.5-11. (a) Measured divergence angle with increasing output power and (b) measured far-field patterns at 40 and 60 mW, simulated far-field pattern at 40 mW.

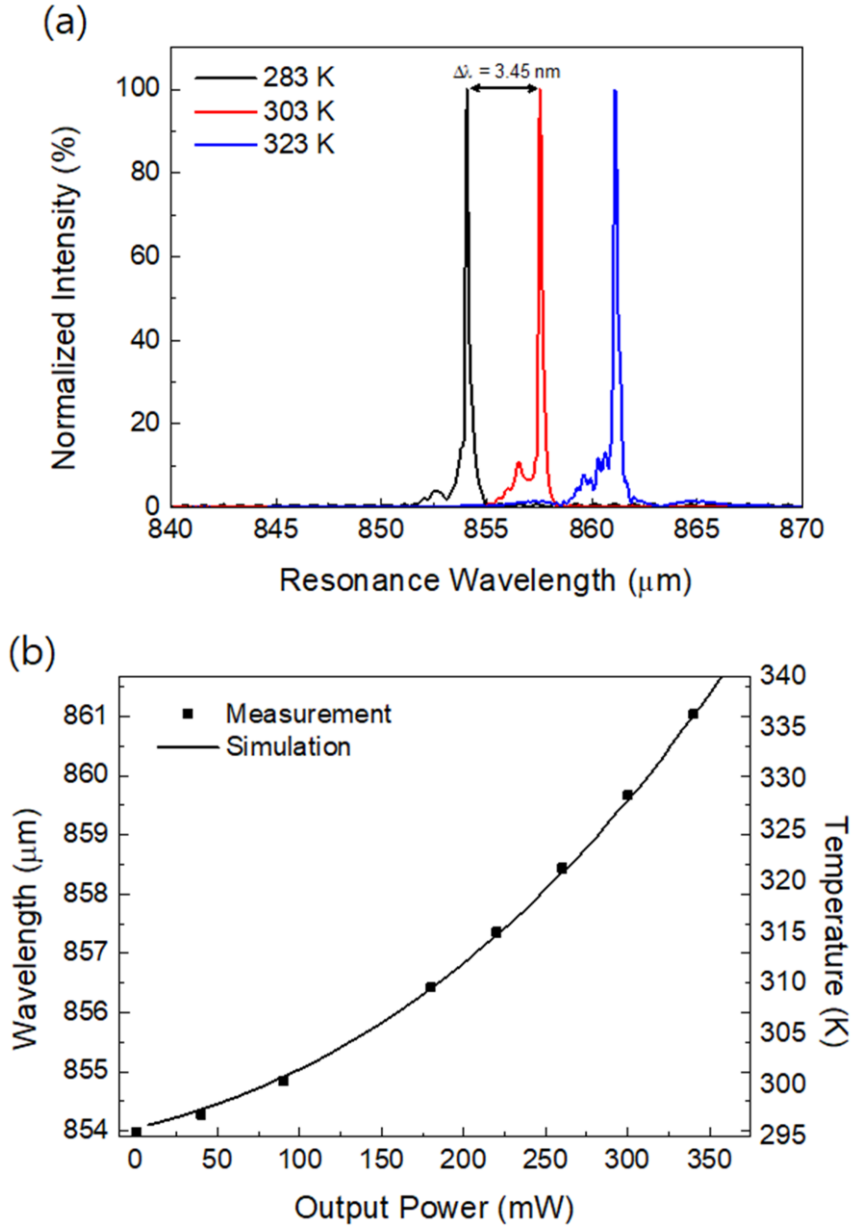


Fig.5-12. Measured (a) Spectrum and (b) measured and simulated inner temperature of  $W = 3 \mu\text{m}$ .

### 5.3. Optimizing Structure

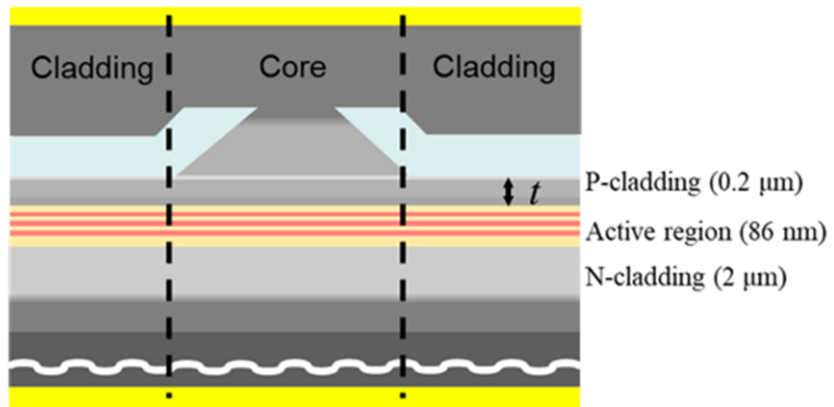
The strategy to suppress the kink involves adjusting the thickness of the layers to inhibit the generation of the 1<sup>st</sup> order mode. Figure 5-13(a) provides a cross-sectional view of the device to illustrate the approach. In the lateral direction, the core and cladding can be distinguished, as shown in the Fig.5-13(a). To suppress the 1<sup>st</sup> order mode, the thickness of the layers is increased to reduce the effective refractive index difference between the core and cladding. The target layers include P-cladding, N-cladding, and the active region. Firstly, the N-cladding layer, with a thickness of 2  $\mu\text{m}$  in the current device, is excluded from consideration as it is already sufficiently thick and may not yield significant effects. Secondly, the active region is excluded from the target because increasing its thickness could negatively impact electrical characteristics and lead to increased heat generation due to higher resistance. Therefore, our focus is on optimizing the thickness of the P-cladding layer to suppress the generation of the 1<sup>st</sup> order mode.

Figure 5-13(b) shows the output power when the thickness of P-cladding ( $t$ ) is increased from 0.2 to 0.95  $\mu\text{m}$ , considering the simulation of the occurrence of the 1<sup>st</sup> order mode. When  $t$  is less than 0.5  $\mu\text{m}$ , it can be observed that the occurrence of the 1<sup>st</sup> order mode is

delayed as intended. However, when  $t$  is greater than  $0.5 \mu\text{m}$ , it is noticed that the optical power at which the 1<sup>st</sup> order mode occurs decreases again. A common aspect among these simulation results is that the maximum temperature inside the quantum well when the 1<sup>st</sup> order mode occurs is approximately 312 K. As  $t$  increases, heat dissipation towards the P-contact side slows down, reaching 312 K at lower powers. Consequently, when  $t$  is greater than 0.5, it is confirmed that the 1<sup>st</sup> order mode occurs more quickly due to the thermal lensing effect. It is evident that around  $t = 0.45$  and  $0.55 \mu\text{m}$ , the first-order mode is best suppressed, allowing for single-mode operation up to approximately 200 mW.



(a)



(b)

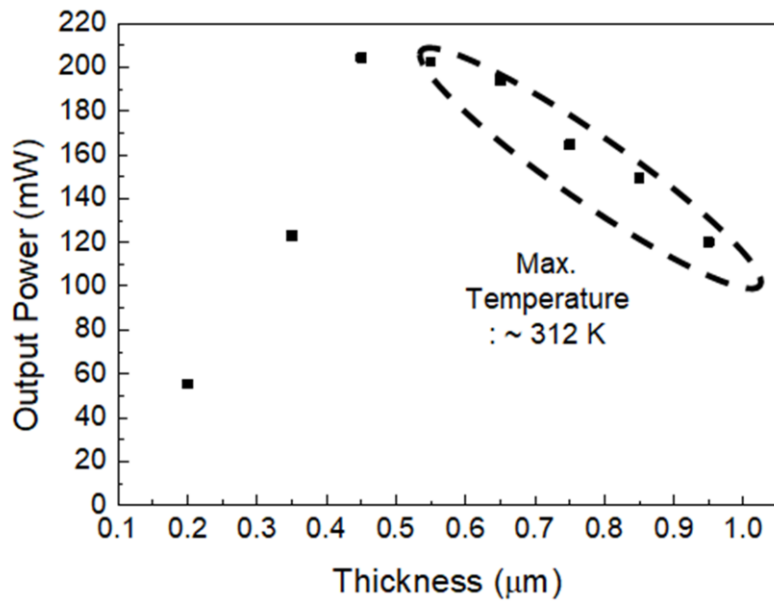


Fig.5-13. (a) Cross sectional diagram and (b) Simulated output power of 1<sup>st</sup> order mode generation with increasing  $t$ .

## 5.4. Summary

In this chapter, we conducted precise simulations to optimize the structure and minimize the kink caused by structural asymmetry in the wet-etching process. To construct accurate simulations, it was necessary to precisely extract and model parameters determining the performance. We achieved this through measurements and the use of DNN (Deep Neural Network). The reliability of the simulation constructed with the extracted parameters was verified through comparisons with actual measured L-I characteristics, far-field patterns, and internal temperature data of the device. With the validated simulation, we were able to optimize the thickness of P-cladding to suppress kink and the occurrence of the 1st order mode.

Since this chapter presents the methodology of model parameters extraction and optimization, it can be applied not only to the devices used in this dissertation but also to other types of semiconductor lasers.

## 6. Conclusion

In this dissertation, we fabricated 850 nm GaAs/AlGaAs-based semiconductor lasers and conducted detailed analyses of the key performance characteristics, L-I characteristics, and beam quality, through measurements and simulations. We set internal loss, Auger, and FCA coefficients as the design parameters determining the L-I characteristics. We obtained an empirical temperature model for internal loss through experimental measurements. Additionally, we employed deep learning to extract and model Auger and FCA coefficients, which were traditionally considered as fitting parameters for simulations. While this dissertation focuses on the results of our specific device, the algorithms and methodologies presented can be applied to other types of semiconductor lasers with an abundant dataset, demonstrating the feasibility of design parameter extraction and modeling.

Furthermore, a detailed analysis of the far-field pattern is crucial to assess beam quality. We analyzed the far-field patterns for various output levels and used these patterns to investigate the nonlinear phenomenon known as kink, which is observed in the L-I characteristics. We also examined the relationship between the internal

temperature of the device and the occurrence of kink. Based on these analyses and the modeled parameters, we proposed structural optimizations aimed at minimizing kink and enhancing beam quality in the fabricated devices.

## Bibliography

- [1] L. J. Walsh, "The current status of laser applications in dentistry", *Aust Dent J.*, vol. 48, no. 3, pp. 146-155, Sep., 2003.
- [2] T. Otani, *et al.*, " Microdrilling and micromachining with diode-pumped solid-state lasers", *Appl. Phys. A*, vol. 79, pp. 1335-1339, Sep., 2004.
- [3] B.Azadgoli, R. Y. Baker, "Laser applications in surgery", *Ann Transl Med.*, vol. 4, no. 23, pp. 1-7, Dec., 2016.
- [4] W. Weiren, *et al.*, "Overview of deep space laser communication", *Sci. China Inf. Sci.*, vol. 61, no. 040301, Apr., 2018.
- [5] M. C. Gower, "Industrial applications of laser micromachining", *Opt. Express*, vol. 7, no. 2, pp. 56-67, 2000.
- [6] P. Crump, *et al.*, "Efficient High-Power Laser Diodes", *IEEE Journal of Selected Topics in Quantum Electronics*, vol. 19, no. 4, pp. 1501211-1501211, July-Aug. 2013.
- [7] D. Xu, *et al.*, "600 W high brightness diode laser pumping source", in *Proceedings of SPIE Photonics West*, vol. 10086, pp. 1008603-1-1008603-6, Feb., 2017.
- [8] M. Kelelmen, *et al.*, "Diode Lasers optimized in Brightness for Fiber Laser Pumping", in *Proceedings of SPIE Photonics West*, vol. 10514, pp. 105140F-1-105140F-8, Feb. 2018.
- [9] G. Sobczak, *et al.*, "Improving the beam quality of high-power laser diodes by introducing lateral periodicity into waveguides", in *Proceedings of SPIE Photonics West*, vol. 8702, pp. 87020B-1-87020B-11, Jan., 2013.

- [10] K. Furuta, *et al.*, "Efficient high-beam-quality operation by use of a diode-stacks-side-pumped quasi-cw Nd:YAG laser", *Advanced Solide-State Lasers*, vol. 50, pp. 15-18, 2001.
- [11] G. An, *et al.*, "Deleterious processes of a diode-pumped cesium vapor hollow-core photonic-crystal fiber laser", *High Power Laser Science and Engineering*, vol. 4, pp. 1-4, Oct., 2016.
- [12] D. A. Vinokurov, *et al.*, "850 nm Diode Lasers Based on AlGaAsP/GaAs Heterostructures", *Semiconductors*, vol. 46, no. 10, pp. 1321-1325, 2012.
- [13] S. Banerjee, *et al.*, "Pushing the boundaries of diode-pumped solid-state lasers for high-energy applications", *High Power Laser Science and Engineering*, vol. 8, pp. 1-3, May, 2020.
- [14] Y. Jeong, *et al.*, "Ytterbium-doped large-core fiber laser with 1.36 kW continuous-wave output power", *Opt. Express*, vol. 12, no. 25, pp. 6088-6092, 2004.
- [15] T. K. Kim, *et al.*, "Evaluation of wavelength-dependent hair growth effects on low-level laser therapy: an experimental animal study", *Lasers Med. Sci.*, vol. 30, pp. 1703-1709, 2015.
- [16] V. Kanappe, *et al.*, "Principles of Lasers and Biophotonic Effects", *Photomedicine and Laser Surgery*, vol. 22, no. 5, pp. 411-417, 2005.
- [17] H. Kawaguchi, "Bistable laser diodes and their applications: state of the art," in *IEEE Journal of Selected Topics in Quantum Electronics*, vol. 3, no. 5, pp. 1254-1270, Oct. 1997.
- [18] H. M. Oubei, *et al.*, "2.3 Gbit/s underwater wireless optical communications using directly modulated 520 nm laser diode", *Opt. Express*, vol. 24, no. 16, pp. 20743-20748, 2015.
- [19] L. Zhong and X. Ma, "Recent developments in high power semiconductor diode lasers," in *Optoelectronics - Devices and*

- Applications*, P. Predeep, ed. (InTech, London, UK, 2011), Chapter 16, pp. 325-348.
- [20] F. Daiminger, *et al.*, "High power laser diodes, laser diode modules and their applications", in *Proceedings of SPIE*, vol. 3682, pp.13-23, Dec., 1998.
- [21] B. L. Volodin, *et al.*, "Wavelength stabilization and spectrum narrowing of high-power multimode laser diodes and arrays by use of volume Bragg gratings", *Opt. Lett.*, vol. 29, no. 16, pp. 1891-1893, 2004.
- [22] T. Zheng, *et al.*, "Frequency-multiplexing photon-counting multi-beam LiDAR", *Photon. Res.*, vol. 7, no. 12, pp. 1381-1385, 2019.
- [23] I. Vornicu, *et al.*, "Design of High-Efficiency SPADs for LiDAR Applications in 110nm CIS Technology," in *IEEE Sensors Journal*, vol. 21, no. 4, pp. 4776-4785, Feb., 2021.
- [24] J. E. Joo, *et al.*, "A CMOS Fully Differential Optoelectronic Receiver for Short-Range LiDAR Sensors," in *IEEE Sensors Journal*, vol. 23, no. 5, pp. 4930-4939, March, 2023.
- [25] S. I. Bae, *et al.*, "Machine-Learned Light-Field Camera that Reads Facial Expression from High-Contrast and Illumination Invariant 3D Facial Images", *Adv. Intell. Syst.*, vol. 4, no. 2100182, pp. 1-9, 2022.
- [26] J. Cheng, *et al.*, "Ultra-compact structured light projector with all-dielectric metalenses for 3D sensing", *AIP Advances*, vol. 9, no. 10, pp. 105016-1-105016-7, Sep., 2019.
- [27] <https://ii-vi.com/product/ses22-9xx-01/>
- [28] <https://www.coherent.com/components-accessories/diode-lasers/single-bars>

- [29] <https://www.rpmclasers.com/product/jold-stack-980-cw-fac-sac-980nm-laser-diode-stack-w-fast-slow-axis-collimation/>
- [30] H. Yang, *et al.*, "Evaluation of beam quality for highpower lasers", in *Proceedings of SPIE*, vol. 6823, pp. 682316-1-682316-6, Feb. 2008.
- [31] Z. Wang, *et al.*, "Fiber coupled diode laser beam parameter product calculation and rules for optimized design", in *Proceedings of SPIE*, vol. 7918, pp. 791809-1-791809-9, Feb. 2011.
- [32] N. Hodgson, *et al.*, "Determination of laser beam parameters with the phase space beam analyser", *Opt. Quant. Electron*, vol.24, pp. S927-S949, April, 1992.
- [33] PICS3D, Crosslight Software Inc. [Online]. Available: [http:// www.crosslight.com](http://www.crosslight.com).
- [34] L. A. Coldren, S. W. Corzine and M. L. Masanovic, *Diode Lasers and Photonic Integrated Circuits*, Jhon Wiley & Sons, Inc. New Jersey, 2012.
- [35] W. Samek, *et al.*, "Explaining Deep Neural Networks and Beyond: A Review of Methods and Applications," in *Proceedings of the IEEE*, vol. 109, no. 3, pp. 247-278, March 2021.
- [36] L. Chen and J. Chen, "Deep Neural Network for Automatic Classification of Pathological Voice Signals", *Journal of Voice*, vol. 36, no. 2, pp. 288.e15-288.e24, March, 2022.
- [37] S. H. Mohammadi and A. Kain, "Voice conversion using deep neural networks with speaker-independent pre-training," *2014 IEEE Spoken Language Technology Workshop (SLT)*, South Lake Tahoe, NV, USA, 2014, pp. 19-23.
- [38] M. H. Tahersima, *et al.*, "Deep Neural Network Inverse Design of Integrated Photonic Power Splitters", *Scientific Reports*, vol.9, pp. 1-9, Feb., 2019.



- [39] S. Mao, et al., "Inverse Design for Silicon Photonics: From Iterative Optimization Algorithms to Deep Neural Networks", *Appl. Sci.*, vol. 11, no. 3822, pp. 1-25, April. 2021.
- [40] K. Kojima, et al., "Deep Neural Networks for Inverse Design of Nanophotonic Devices", *J. Lightwave Techno.*, vol. 39, no. 4, pp. 1010-1019, 2021.
- [41] D. Luo, L. Xia, C. Zhang and L. Wang, "Automatic Pronunciation Evaluation in High-states English Speaking Tests Based on Deep Neural Network Models," *2019 2nd International Conference on Artificial Intelligence and Big Data (ICAIBD)*, Chengdu, China, 2019, pp. 124-128.
- [42] Y. Gu, *et al.*, "Beam shaping technology for High power diode laser source", *Advanced Materials Research*, vol. 915-916, pp. 385-389, April 2014.
- [43] V. Rossin, *et al.*, "High power, high brightness diode lasers for kW lasers systems," in *Proceedings of 2015 IEEE High Power Diode Lasers and Systems Conference (HPD)*, pp. 35-36, Oct. 2015.
- [44] A. Bachmann, *et al.*, "Continued Improvement in Reduced-mode (REM) Diodes Enable 272 W from 105  $\mu\text{m}$  0.15 NA Beam", in *Proceedings of SPIE*, vol. 10086, pp. 1008602-1-1008602-9, Feb. 2017.
- [45] M. Kanskar, *et al.*, "Recent brightness improvements of 976 nm high power laser bars", in *Proceedings of SPIE*, vol. 10086, pp. 1008609-1-1008609-6, Feb. 2017.
- [46] E. I. Kotova, *et al.*, "Efficiency analysis of optical schemes for the development of high power laser diode modules", in *Proceedings of SPIE*, vol. 10695, pp. 10695T-1-10695T-12, May 2018.
- [47] A. Pietrzak, *et al.*, "Development of highly efficient laser diodes emitting around 1060nm for medical and industrial applications", in

- Proceedings of SPIE*, vol. 10900, pp. 109000K-1-109000K-9, March 2019.
- [48] H. Wu, *et al.*, "Design of a fiber coupled diode laser based on a novel beam shaping component which is provided with beam collimating and re-orienting", in *Proceedings of SPIE*, vol. 11437, pp. 114370W-1-114370W-7, March 2020.
- [49] J. Su, *et al.*, "Beam waist shrinkage of high-power broad-area diode lasers by mode tailoring", *Opt. Express*, vol. 28, pp. 13131-13140, 2020.
- [50] X. Liu, *et al.*, "Demonstration of High Brightness and Reliability at 20 W from a 976 nm, 150  $\mu\text{m}$  Emitter Width Laser Diode," in *Proceedings of 2021 27th International Semiconductor Laser Conference (ISLC)*, pp. 1-2, Oct. 2021.
- [51] S. McDougall, *et al.*, "Operation of wide emitter 976 nm fiber laser pump chips with high reliability and temperature stability," in *Proceedings of 2022 28th International Semiconductor Laser Conference (ISLC)*, pp. 1-2, Oct. 2022.
- [52] P. Crump, *et al.*, "Progress in experimental studies into the beam parameter product of GaAs-based high-power diode lasers", in *Proceedings of SPIE*, vol. 11983, pp. 1198307-1-1198307-10, March 2022.
- [53] X. Liu, *et al.*, "High-power semiconductor laser chips for fiber-laser-based Lidar pump applications", in *Proceedings of SPIE*, vol. 12403, pp. 1240309-1-1240309-7, March 2023.
- [54] M. Winterfeldt, *et al.*, "Beam waist shrinkage of high-power broad-area diode lasers by mode tailoring", in *Proceedings of 2015 European Conference on Lasers and Electro-Optics - European Quantum Electronics Conference*, pp. CB\_P\_5, 2015..

- [55] R. K. Huang, *et al.*, "Recent progress on high-brightness kW-class direct diode lasers," in *Proceedings of 2015 IEEE High Power Diode Lasers and Systems Conference (HPD)*, pp. 29-30, Oct. 2015.
- [56] M. Kanskar, *et al.*, "High-brightness diodes and fiber-coupled modules", in *Proceedings of SPIE*, vol. 9348, pp. 934804-1-934804-9, March 2015.
- [57] Y. Qi, *et al.*, "Design of 150W, 105- $\mu\text{m}$ , 0.22NA, fiber-coupled laser diode module by ZEMAX", in *Proceedings of SPIE*, vol. 10152, pp. 101521H-1-101521H-9, Oct. 2016.
- [58] Y. Junhong, *et al.*, "High-brightness laser-diode device emitting 500 W from a 200  $\mu\text{m}$ /NA0.22 fiber", *Optics & Laser Technology*, vol. 80, pp. 92-97, Jan. 2016.
- [59] T. Wang, *et al.*, "Injection-insensitive lateral divergence in broad-area diode lasers achieved by spatial current modulation", *Appl. Phys. Express*, vol. 9, no. 112102, pp. 112102-1-112102-4, Jan. 2016.
- [60] A. Bayer, *et al.*, "Multi-kW high-brightness fiber-coupled diode laser based on two-dimensional stacked tailored diode bars", in *Proceedings of SPIE*, vol. 9733, pp. 97330A-1-97330A-6, March 2016.
- [61] X. Wang, *et al.*, "Researching the 915 nm high-power and high-brightness semiconductor laser single-chip coupling module", *J. Semicond.*, vol. 38, no. 2, pp. 024006-1-024006-4, Feb. 2016.
- [62] A. Pietrzak, *et al.*, "Development of highly-efficient laser diodes emitting at around 1060nm", in *Proceedings of SPIE*, vol. 10086, pp. 100860J-1-100860J-10, Feb. 2017.
- [63] Q. Fang, *et al.*, "5 kW Near-Diffraction-Limited and 8 kW High-Brightness Monolithic Continuous Wave Fiber Lasers Directly

- Pumped by Laser Diodes", *IEEE Photonics Journal*, vol. 9, no. 5, pp. 1-7, Oct. 2017.
- [64] D. Xu, *et al.*, "High brightness KW-class direct diode laser", in *Proceedings of SPIE*, vol. 10514, pp. 105140N-1-105140N-6, Feb. 2018.
- [65] C. Bree, *et al.*, "Beam-combining scheme of high-power broadarea semiconductor lasers with Lyot-filtered reinjection: modeling, simulations, and experiments", *Journal of the Optical Society of America B*, vol. 36, no. 7, pp. 1721-1730, July 2019.
- [66] J. Tian, *et al.*, "High power diode laser source with a transmission grating for two spectral beam combining", *Optik*, vol. 192, pp. 1-4, Sep. 2019.
- [67] J. Su, *et al.*, "Selective loss tailoring of broad-area diode lasers", *Jpn. J. Appl. Phys.*, vol. 60, pp. 020901-1-020901-5, Jan. 2021.
- [68] T. Li, *et al.*, "Design of a 976nm 190-W fibercoupled laser diode", in *Proceedings of SPIE*, vol. 12311, pp. 123110E-1-123110E-7, Dec. 2022.
- [69] V. V. Bezotosnyi, *et al.*, "Thermal modelling of high-power laser diodes mounted using various types of submounts", *Quantum Electronics*, vol. 44, no. 10, pp. 899-902, 2014.
- [70] W. pittroff, *et al.*, "Mounting of Laser Bars on Copper Heat Sinks Using Au/Sn Solder and CuW Submounts", *52nd Electronic Components and Technology Conference 2002. (Cat. No.02CH37345)*, San Diego, CA, USA, 2002, pp. 276-281.
- [71] H. Zhang, *et al.*, "Effect of submount thickness on near-field bowing of laser diode arrays", *Appl. Opt.*, vol. 57, no. 28, pp. 8407-8411, Oct., 2018.

- [72] V. P. Gordeev, *et al.*, "Thermoelastic stresses in high-power CW diode laser arrays assembled on CuW and AlN submounts", *Quantum Electron.*, vol. 52, no. 5, pp.443-448, 2022.
- [73] J. Piprek, Z. M. S. Li, "On the importance of non-thermal far-field blooming in broad-area high-power laser diodes", *Appl. Phys. Lett.*, vol 102, no. 22, pp. 221110-1-221110-4, 2013.
- [74] J. Bai, *et al.*, "Mitigation of thermal lensing effect as a brightness limitation of high-power broad area diode lasers", in *Proceedings of SPIE*, vol. 7953, pp. 79531F-1-79531F-7, Feb., 2011.
- [75] J. Piprek, "Self-consistent analysis of thermal far-field blooming of broad-area laser diodes", *Opt. Quant. Electron.*, vol. 45, pp. 581-588, 2013.
- [76] W. Sun, *et al.*, "Higher brightness laser diodes with smaller slow axis divergence", in *Proceedings of SPIE*, vol. 8605, pp. 86050D-1-86050D-9, Feb., 2013.
- [77] J. Piprek, "Inverse Thermal Lens Effects on the Far-Field Blooming of Broad Area Laser Diodes," in *IEEE Photonics Technology Letters*, vol. 25, no. 10, pp. 958-960, May15, 2013.
- [78] Y. Kim, *et al.*, "High-power broad-area laser diode performance improvement with a double pedestal structure", *Jpn. J. Appl. Phys.*, vol. 58, pp. 042004-1-042004-6, Feb., 2019.
- [79] S.G. Strohmaier, *et al.*, "Forward development of kW-class power diode laser bars", in *Proceedings of SPIE*, vol. 10514, pp. 1051409-1-1051409-6, May, 2018.
- [80] [https://www.thorlabs.com/newgrouppage9.cfm?objectgroup\\_id=4737](https://www.thorlabs.com/newgrouppage9.cfm?objectgroup_id=4737).
- [81] Y. Ben, Changzheng Sun, Song Xue, Yi Luo, T. Yagi and E. Omura, "Nonlinearity in power-current Characteristics of narrow-pulse-

- driven AlGaInP laser diodes," in *IEEE Journal of Quantum Electronics*, vol. 40, no. 4, pp. 349-353, April, 2004.
- [82] J. Guthrie *et al.*, "Beam instability in 980-nm power lasers: experiment and analysis," in *IEEE Photonics Technology Letters*, vol. 6, no. 12, pp. 1409-1411, Dec., 1994.
- [83] Y. Kaifuchi, *et al.*, "Enhanced power conversion efficiency in 900-nm range single emitter broad stripe laser diodes maintaining high power operability", in *Proceedings of SPIE*, vol. 10900, pp. 109000F-1-109000F-6, March, 2019.
- [84] P. Crump, *et al.*, "85% power conversion efficiency 975-nm broad area diode lasers at  $-50^{\circ}\text{C}$ , 76 % at  $10^{\circ}\text{C}$ ," *2006 Conference on Lasers and Electro-Optics and 2006 Quantum Electronics and Laser Science Conference*, Long Beach, CA, USA, 2006, pp. 1-2.
- [85] M. Kanskar, *et al.*, "High-power conversion efficiency Alfree diode lasers for pumping highpower solid-state laser systems", in *Proceedings of SPIE*, vol. 5738, pp. 47-56, April, 2005.
- [86] L. Wang, *et al.*, "High Power Conversion Efficiency Narrow Divergence Angle Photonic Crystal Laser Diodes," in *IEEE Photonics Journal*, vol. 14, no. 4, pp. 1-6, Aug. 2022.
- [87] L. Wang *et al.*, "High-power laser diode at 9xx nm with 81.10% efficiency", *Opt. Lett.*, vol. 47, no. 13, pp. 3231-3234, 2022.
- [88] A. Bachmann, *et al.*, "Recent brightness improvements of 976 nm high power laser bars", in *Proceedings of SPIE*, vol. 10086, pp. 1008602-1-1008602-9, Feb., 2017 .
- [89] Z. Wang, *et al.*, "High power, high efficiency continuous-wave 808 nm laser diode arrays", *Optics and Laser Technology*, vol.97, pp. 297-301, 2017.

- [90] C. -e. Zah, *et al.*, "Low SMILE vertically stacked laser bars enable kW modular line lasers," *2017 IEEE High Power Diode Lasers and Systems Conference (HPD)*, Coventry, UK, 2017, pp. 9-10.
- [91] G. Liu, *et al.*, "High power single lateral mode 1050 nm laser diode bar", in *Proceedings of SPIE*, vol.10086, pp. 100860Y-1-100860Y-6, Feb. 2017.
- [92] R. Paoletti, *et al.*, "350 W high-brightness multi-emitter semiconductor laser module emitting at 976 nm", in *Proceedings of SPIE*, vol. 11668, pp. 1166805-1-1166805-7, March, 2021.
- [93] P. Hildenstein, *et al.*, "High power, high beam quality miniaturized diode laser module for direct material processing around 980 nm", in *Proceedings of SPIE*, vol. 11668, pp. 1166804-1-1166804-7, March. 2021.
- [94] J. Piprek, P. Abraham and J. E. Bowers, "Cavity length effects on internal loss and quantum efficiency of multiquantum-well lasers," in *IEEE Journal of Selected Topics in Quantum Electronics*, vol. 5, no. 3, pp. 643-647, May-June 1999.
- [95] H. Y. Ryu, *et al.*, "Determination of internal parameters in blue InGaN laser diodes by the measurement of cavity-length dependent characteristics", *Appl. Phys. Lett.*, vol. 93, no. 1, pp. 011105-1-011105-3, July, 2008.
- [96] D. A. Veselov, *et al.*, "Measurements of internal optical loss inside an operating laser diode", *J. Appl. Phys.*, vol. 126, no. 21, pp. 213107-1-213107-8, Dec., 2019.
- [97] J. Piprek, P. Abraham and J. E. Bowers, "Self-consistent analysis of high-temperature effects on strained-layer multiquantum-well InGaAsP-InP lasers," in *IEEE Journal of Quantum Electronics*, vol. 36, no. 3, pp. 366-374, March, 2000

- [98] T. Koike-Akino, *et al.*, "Neural Turbo Equalization: Deep Learning for Fiber-Optic Nonlinearity Compensation", *J. Lightwave Technol.*, vol. 38, no. 11, pp. 3059-3066, 2020.
- [99] F. Li, *et al.*, "The DNN-based DBP scheme for nonlinear compensation and longitudinal monitoring of optical fiber links", *Digital Communications and Networks*, 2023.
- [100] Y. Rivenson, *et al.*, "Phase recovery and holographic image reconstruction using deep learning in neural networks", *Light Sci. Appl.*, vol. 7, no.17141, pp. 1-9, Oct., 2017.
- [101] B. Yao, *et al.*, "Image reconstruction with a deep convolutional neural network in high-density super-resolution microscopy", *Opt. Express*, vol. 28, no. 10, pp. 15432-15446, 2020.
- [102] X. Han, *et al.*, "Inverse design of metasurface optical filters using deep neural network with high degrees of freedom", *InfoMat.*, vol.3, pp. 432-442, June, 2020.
- [103] T. Zhao *et al.*, "Highly Efficient Inverse Design of Semiconductor Optical Amplifiers Based on Neural Network Improved Particle Swarm Optimization Algorithm," in *IEEE Photonics Journal*, vol. 15, no. 2, pp. 1-9, April, 2023.
- [104] Z. Ma, *et al.*, "Inverse design of semiconductor laser parameters based on deep learning and particle swarm optimization method", in *Proceedings of SPIE*, vol. 11209, pp.112092X-1-112092X-7, Dec., 2019.
- [105] Z. Ma, *et al.*, "Parameter extraction and inverse design of semiconductor lasers based on the deep learning and particle swarm optimization method", *Opt. Express*, vol. 28, no. 15, pp. 21971-21981, July, 2020.



- [106] J. R. Meyer, *et al.*, "Comparison of Auger Coefficients in Type I and Type II Quantum Well Midwave Infrared Lasers," in *IEEE Journal of Quantum Electronics*, vol. 57, no. 5, pp. 1-10, Oct. 2021.

## Abstract (In Korean)

# 850 nm GaAs/AlGaAs 반도체 레이저의 디자인 파라미터 모델링 및 빔 품질 분석

본 학위 논문은 850 nm GaAs/AlGaAs 기반의 반도체 레이저의 출력뿐 아니라 빔 품질 향상을 위한 소자 구조연구와 시뮬레이션 기반의 구조 최적화 연구의 방법론적인 연구에 중점을 두고 있다. 반도체 레이저의 경우 대량양산이 가능하여 cost effective하며, 크기가 작아 다양한 광원이 필요한 시스템에서 사용되고 있다. 하지만 고출력 반도체 레이저는 다 수의 멀티 모드의 발생으로 인해 빔 품질이 나쁘다는 단점을 가지고 있기 때문에 고출력을 요하는 시스템에서는 직접적으로 사용하지 못하고 가스, 섬유 레이저 등의 다른 레이저의 펌핑 소스로써의 역할을 하고 있다. 반도체 레이저가 고출력을 달성하면서 동시에 가스나 광섬유 레이저와 동등한 빔 품질을 갖추게 되면, 직접적인 활용이 가능해져 에너지 손실을 크게 감소시킬 수 있다. 또한, 기존 반도체 레이저의 장점을 통해 기존 레이저를 사용한 시스템에서 비용 및 크기 효율이 현격히 향상될 것으로 기대되어 이를 연구하는 동기가 되었다.

고출력 반도체 레이저의 경우 출력이 커질수록 빔 품질이

저하되는 far-field blooming이 발생하는데, 우리는 위, 아래 중심부로 효율적으로 열 방출이 가능한 double pedestal 구조를 고안하여 광 출력과 빔 품질이 향상된 결과를 얻었다. 또한, 싱글 모드 반도체 레이저(SMSL)로 이루어진 레이저 바를 통해 고출력을 달성하고, 일반적인 고출력 반도체 레이저의 다중 모드로 인한 빔 품질 저하 문제를 해결하기 위해 850 nm GaAs/AlGaAs SMSL을 제작하고 분석하였다. 목표로 했던 1 W에 근접한 최대 출력을 가지는 소자를 제작하였으나, 비선형현상인 kink로 인한 빔 품질저하가 발생하여, 이를 해결하고자 구조최적화 연구를 같이 진행하였다. 구조최적화에 필요한 정밀한 시뮬레이션을 구성하기 위해, 성능을 결정짓는 디자인 파라미터들을 측정 및 덤 러닝을 통해 정확하게 추출 및 모델링을 진행하였다. 구성된 시뮬레이션을 측정값과의 비교를 통해 신뢰성을 검증하고 kink가 최대한 억제된 최적화된 구조를 제안한다. 최적화 연구는 본 논문에 사용된 소자뿐만이 아니라 다른 소자에서도 일관성 있게 적용될 수 있을 것으로 기대된다.

---

**핵심 단어:** 반도체 레이저, double Pedestal, SMSL, 덤 러닝, DNN, 디자인 파라미터 추출, L-I 특성, 내부 손실, Auger 상수, FCA 상수, kink, far-field 패턴, 빔 퀄리티.

## List of Publications

### *International Journal Papers*

- [1] **Jung-Tack Yang**, Younghyun Kim, Marzieh Pournoury, Jae-Bong Lee, Dong-Soo Bang, Tae-Kyung Kim, and Woo-Young Choi, “Influence of Emitter Width on the Performance of 975-nm (In,Ga)(As,P)/(Al,Ga)As High-power Laser Diodes”, *Current Optics and Photonics*, Vol. 3, No. 5, pp. 445-450, Oct. 2019.
- [2] **Jung-Tack Yang**, Jung-Geun Kwak, An-Sik Choi, Tae-Kyung Kim, and Woo-Young Choi, “Lateral Far-field Characteristics of Narrow-width 850 nm High Power GaAs/AlGaAs Laser Diodes”, *Current Optics and Photonics*, Vol. 6, No.2, pp. 191-195, Apr. 2022.
- [3] Younghyun Kim, **Jung-Tack Yang**, and Woo-Young Choi, “High-power broad-area laser diode performance improvement with a double pedestal structure”, *Japanese Journal of Applied Physics*, Vol. 58, pp. 042004-1 - 042004-6, March 2019.
- [4] Daehong Kim, **Jung-Tack Yang**, Woo-Young Choi, and Younghyun Kim, “Improved Far-Field Angle in Narrow-Ridge High-Power Laser Diodes Using a Double Stripe Structure”, *IEEE Photonics Journal*, Vol. 15, pp. 1-7, Dec. 2023.

## *Domestic Journal Papers*

- [1] 양정택, 곽정근, 최안식, 김태경, 최우영, “850 nm GaAs/AlGaAs MQW LD의 Lateral-mode 특성 연구”, 한국광학회지, Vol. 32, No. 2, pp. 55-61, Apr. 2021

## ***International Conference Presentations***

- [1] **Jung-Tack Yang**, Younghyun Kim, Jae-Bong Lee, Dong-Soo Bang, Tae-Kyung Kim and Woo-Young Choi, “Dependence of High-Power Laser Diode Performance on Emitter Width”, to be presented in *SPIE Photonics West*, Feb. 2019, California, USA.
- [2] **Jung-Tack Yang**, Hyewon Han and Woo-Young Choi, “Model parameters extraction for 850 nm GaAs/AlGaAs laser diodes using simple deep neural network”, to be presented in *SPIE Photonics West*, Jan. 2024, California, USA.
- [3] Younghyun Kim, Yunsu Sung, **Jung-Tack Yang**, and Woo-Young Choi, “Simulation of high-power laser diode with improved heat sinking structure using epitaxial liftoff technique”, to be presented in *SPIE Photonics West*, Jan.-Feb. 2018, California, USA.

## ***Domestic Conference Presentations***

- [1] 양정택, 한혜원, 곽정근, 최안식, 김태경, 강홍구, 최우영, “딥 러닝을 통한 레이저 다이오드 파라미터 추출”, 제29회 광전자 및 광통신 학술대회 (COOC 2022), May 2022, 부산.
- [2] 양정택, 곽정근, 최안식, 김태경, 최우영, “Cs 알칼리 레이저 펌핑을 위한 레이저다이오드 ( $\lambda=850$  nm) 핵심 파라미터 추출”, 2020 한국군사과학기술학회 종합학술대회, Nov. 2020, online.
- [3] 양정택, 곽정근, 최안식, 김태경, 최우영, “850nm GaAs/AlGaAs 레이저 다이오드의 internal loss 및 quantum efficiency 값 추출 및 이를 이용한 simulation 정확도 향상”, 2019 Photonics Conference, Dec. 2019, 평창.
- [4] 양정택, 이재봉, 방동수, 김태경, 최우영, “온도 의존성 parameter를 활용한 975 nm 고출력 레이저 다이오드의 정확한 Simulation”, 2018 Photonics Conference, Dec. 2018, 평창.
- [5] 양정택, 김영현, 최우영, “고출력 레이저 다이오드에서 Thermal lensing이 Far field에 끼치는 영향”, 2017 Photonics Conference, Nov. 2017, 제주도.

